

# **Field Line Resonance in Two and a Half Dimensions**

**DRAFT VERSION CREATED ON MARCH 12, 2016**

© Charles A. McEachern 2016  
ALL RIGHTS RESERVED

# Acknowledgements

Acknowledgement placeholder.

# Dedication

Dedication placeholder.

## Abstract

Something something Pc4 pulsations. Ultra low frequency (ULF) waves with periods of a minute or two. They correspond to field line resonances near Earth's plasmapause. Drift or drift-bounce resonance with energetic radiation belt and ring current particles. Radial diffusion.

Pc4 pulsations are known to exhibit different behavior based on their azimuthal mode-number. Low- $m$  Pc4 pulsations are driven at the outer edge of the magnetosphere, and have a compressional component. High- $m$  Pc4 pulsations are non-compressional and are driven within the magnetosphere.

Giant pulsations are a subset of high- $m$  Pc4 pulsations which are of particular interest. High- $m$  Pc4 pulsations are hard to simulate. Traditionally, simulations are driven from the outer boundary, which doesn't work in this case. And resolving high azimuthal modenumber is computationally expensive in a 3D simulation.

Chapter 1 gives a general introduction is made to Earth's magnetosphere. Also summarizes Pc4 pulsations in terms of prominent theoretical and observational work, including work on giant pulsations. (Note: this mostly doesn't exist yet.)

Chapter 2 presents a 2.5D model designed to simulate Pc4 pulsations, including those with high azimuthal modenumber. The model is built upon recent work by Lysak, and includes a dipole-aligned geometry, a height-resolved ionosphere, and coupling to a conducting Earth. Ring current modulation is introduced as a novel driving mechanism. Also investigates the results of adding electron inertial effects to the model, allowing the computation of parallel electric fields and field-aligned currents. It also derives dispersion relations for a cold, resistive plasma, such as Earth's inner magnetosphere and ionosphere. This gives an idea as to the waves expected to be produced.

Chapter 3 showcases changes in Pc4 behavior as a result of altering the azimuthal modenumber. This includes a rotation of poloidal to toroidal waves, significantly refining past work by Mann, and before that Radoski. (There are a lot of figures here. It might

end up being two chapters.)

Chapter 4 compares model output to poloidal Pc4 observations made with the Van Allen Probes. (Note: this hasn't quite happened yet. The chapter briefly explains.)

Chapter 5 offers a summary and possibilities for future work.

NOTE: ALL FIGURES ARE PDFS. Some of the frames are small, but they should remain sharp when you zoom in on them.

# Contents

<b>Acknowledgements</b>	i
<b>Dedication</b>	ii
<b>Abstract</b>	iii
<b>List of Tables</b>	viii
<b>List of Figures</b>	ix
<b>1 Introduction</b>	1
1.1 The Near-Earth Environment . . . . .	3
1.1.1 The Outer Magnetosphere . . . . .	3
1.1.2 The Inner Magnetosphere . . . . .	4
1.1.3 The Ionosphere . . . . .	4
1.2 Geomagnetic Disturbances . . . . .	6
1.2.1 Storms . . . . .	6
1.2.2 Substorms . . . . .	6
1.3 Field Line Resonance . . . . .	7
1.3.1 Structure and Jargon . . . . .	13
1.3.2 Giant Pulsations . . . . .	15
1.3.3 Motivations for the Present Work . . . . .	16
<b>2 Model</b>	18
2.1 Dispersion Relation . . . . .	19

2.1.1	Guided Propagation . . . . .	20
2.1.2	Compressional Propagation . . . . .	22
2.1.3	High Altitude Limit . . . . .	23
2.1.4	Implications to the Present Work . . . . .	24
2.2	“Tuna Half” Dimensional Simulation . . . . .	27
2.2.1	Physical Parameter Profiles . . . . .	28
2.2.2	Coordinate System . . . . .	30
2.2.3	Driving . . . . .	34
2.2.4	Maxwell’s Equations . . . . .	37
2.2.5	Boundary Conditions . . . . .	41
2.3	Electron Inertial Effects . . . . .	46
2.3.1	The Boris Factor . . . . .	47
2.3.2	Parallel Currents and Electric Fields . . . . .	49
2.3.3	Inertial Length Scales . . . . .	52
2.3.4	Field-Aligned Current . . . . .	53
<b>3</b>	<b>Results</b>	<b>56</b>
3.1	Finite Poloidal Lifetimes . . . . .	57
3.1.1	High Conductivity . . . . .	58
3.1.2	Low Conductivity . . . . .	60
3.2	Spatial Distribution of Energy . . . . .	63
3.2.1	Resonant Driving . . . . .	65
3.2.2	Nonresonant Driving . . . . .	68
3.3	Significance for Giant Pulsations . . . . .	70
3.3.1	Ground Signatures . . . . .	70
<b>4</b>	<b>Observations</b>	<b>73</b>
4.1	Event Selection . . . . .	74
4.1.1	Identifying the Fundamental Harmonic . . . . .	74
4.1.2	Bias in MLT . . . . .	74
4.2	Something Something Results . . . . .	75
4.2.1	Something Something Results . . . . .	77

<b>5 Conclusion</b>	<b>78</b>
5.1 Summary of Results . . . . .	79
5.2 Future Work . . . . .	80
<b>References</b>	<b>81</b>
<b>Appendix A. Differential Geometry</b>	<b>93</b>
A.1 Glossary . . . . .	93
A.2 Acronyms . . . . .	93

# List of Tables

1.1	Integrated Ionospheric Conductivity . . . . .	5
1.2	IAGA Magnetic Pulsation Frequency Bands . . . . .	8
2.1	Integrated Atmospheric Conductivity . . . . .	42
A.1	Acronyms . . . . .	93

# List of Figures

1.1	Alfvén Bounce Frequency Profiles . . . . .	10
2.1	Compressional Alfvén Wave Cutoff Frequencies . . . . .	26
2.2	Alfvén Speed Profiles . . . . .	29
2.3	Ionospheric Conductivity Profiles . . . . .	30
2.4	Nonorthogonal Dipole Grid . . . . .	34
2.5	Decreasing Penetration with Increasing Modenumber . . . . .	36
2.6	Sym-H for June 2013 Storm . . . . .	37
2.7	Plasma Frequency Profile . . . . .	47
2.8	Electric Field Snapshots . . . . .	49
2.9	Current and Poynting Flux at the Ionosphere . . . . .	51
2.10	Power Density at the Ionosphere . . . . .	52
2.11	Parallel Electric Fields by Perpendicular Grid Resolution . . . . .	53
3.1	Poloidal and Toroidal Energy: Active Day . . . . .	59
3.2	Poloidal and Toroidal Energy: Quiet Night . . . . .	61
3.3	Poloidal and Toroidal Energy Distribution: Resonant Driving . . . . .	65
3.4	Poloidal and Toroidal Energy Distribution: Nonresonant Driving . . . . .	68
3.5	Dayside Ground Magnetic Fields . . . . .	71

# Chapter 1

## Introduction

**TODO:** In 1859, humanity was working hard to get its shit together. The United States moved steadily toward the American Civil War, which would abolish slavery and consolidate the power of the federal government. A slew of conflicts in Southern Europe, such as the Austro-Sardinian War, set the stage for the unification of Italy. The Taiping Civil War – one of the bloodiest conflicts of all time – is considered by many to mark the beginning of modern Chinese history. Origin of Species was published. The first transatlantic telegraph cable was laid.

Meanwhile, ambivalent to humanity, the Sun belched an intense burst of charged particles and magnetic energy directly at Earth. The resulting geomagnetic storm<sup>1</sup> caused telegraph systems to fail across the Western hemisphere[37], electrocuting some operators. Displays of the northern lights were visible as far south as Cuba.

The Solar Storm of 1859 was perhaps the most powerful in recorded history, but by no means was it a one-time event. The Sun discharges hundreds of coronal mass ejections (CMEs) per year, of all sizes, in all directions. In fact, a comparably large CME narrowly missed Earth in 2012[77]. Had it not, it's estimated[73] that it would have caused widespread, long-term electrical outages, with a damage toll on the order of  $10^9$  dollars.

---

<sup>1</sup>The Solar Storm of 1859 is also called the Carrington Event, after English astronomer Richard Carrington. He drew a connection between the storm's geomagnetic activity and the sunspots he had observed the day before.

The Sun’s extreme – and temperamental – effect on Earth’s magnetic environment makes a compelling case for the ongoing study of space weather. Such research has evolved over the past century from sunspot counts and compass readings to multi-satellite missions and supercomputer simulations. Modern methods have dramatically increased humanity’s understanding of the relationship between the Sun and the Earth; however, significant uncertainty continues to surround geomagnetic storms, substorms, and the various energy transport mechanisms that make them up.

The present work focuses in particular on the phenomenon of field line resonance: Alfvén waves bouncing between the northern and southern hemispheres. Such waves play an important part in the energization of magnetospheric particles, the transport of energy from high to low altitude, and the driving of currents at the top of the atmosphere.

## 1.1 The Near-Earth Environment

From Earth's surface to about 100 km, the atmosphere is a well-behaved fluid: a collisional ensemble of neutral atoms. However, beyond there, its behavior changes dramatically. As altitude increases, solar ultraviolet radiation becomes more intense, which ionizes atmospheric atoms. Density also decreases, slowing collisional recombination. Whereas the neutral atmosphere is held against Earth's surface by gravity, the behavior of charged particles is dominated by Earth's geomagnetic field... and the electromagnetic disturbances created as that field is hammered by the solar wind.

TODO: Neutral density is larger than charged particle density (?) but it doesn't matter because mean free path is huge.

The present section outlines the structure of the magnetosphere; that is, the region of space governed primarily by Earth's magnetic field. Particular emphasis is placed on structures which relate closely to field line resonance.

### 1.1.1 The Outer Magnetosphere

During quiet times<sup>2</sup>, the behavior of the magnetosphere is driven by the solar wind: a hot, rarefied, fast-moving solar outflow threaded by the Sun's magnetic field<sup>3</sup>.

The magnetosphere's outer boundary represents a balance between the solar wind dynamic pressure and the magnetic pressure of Earth's dipole field. On the dayside, the dipole is compressed, pushing the magnetopause to within  $10 R_E$ <sup>4</sup> of Earth. The nightside magnetosphere is stretched into a long tail which may exceed  $50 R_E$  in width and  $100 R_E$  in length.

Consistent with Ampère's Law, the interplanetary magnetic field is separated from the

---

<sup>2</sup>Geomagnetically active times are the topic of Section 1.2

<sup>3</sup>Usual solar wind velocities, densities, and temperatures fall on the order of 100 km/s,  $10 \text{ cm}^{-3}$ , and 1 keV respectively. At Earth's orbit, the Sun's magnetic field has a magnitude around 1 nT.

<sup>4</sup>Distances in the magnetosphere are typically measured in units of Earth radii:  $1 R_E \equiv 6378 \text{ km}$ .

magnetosphere by a current sheet: the magnetopause. On the dayside, the magnetopause current flows duskward; on the nightside, it flows downward around the magnetotail.

Plasma within the tail is cool ( $\sim 100$  eV) and rarefied ( $\sim 10^{-2}$  /cm<sup>3</sup>). Earth's dipole is significantly deformed in the magnetotail; the magnetic field in the northern lobe of the tail points more or less Earthward, and vice versa. The two lobes are divided by the plasma sheet, which is comparably hot ( $\sim 1$  keV) and dense ( $\sim 1$  /cm<sup>3</sup>). The plasma sheet carries a duskward current which connects to the magnetopause current.

TODO: Open vs closed field lines.

TODO: Magnetic flux freezing.

TODO: Reconnection. Slow accumulation of energy in the tail.

### 1.1.2 The Inner Magnetosphere

Within about  $10 R_E$  of Earth, the dipole magnetic field is not appreciably deformed by the solar wind.

TODO: Get a better number than  $10 R_E$ , either for here or for the position of the magnetopause.

TODO: Radiation belts. One at  $L \sim 2$  and another around  $L \sim 5$ .  $T \sim 10^5$  eV to  $10^6$  eV.  
Density... Radial diffusion...

TODO: Plasmasphere. Out to  $L \sim 4$ . Density ranges  $1$  /cm<sup>3</sup> to  $10^4$  /cm<sup>3</sup>. Cold:  $T \sim 1$  eV.  
Plasmapause location is set by balance between...

TODO: Ring current.  $L \sim 2$  to 9.  $T \sim 10^3$  eV to  $10^5$  eV. Density... Dst...

### 1.1.3 The Ionosphere

TODO: Is this its own section, or should it be folded in with the inner magnetosphere?

TODO: “Sweet spot” where there is a charged population and also a nonzero perpendicular conductivity. Ionospheric currents create magnetic field signatures on the ground.

TODO: Convection electric field, and two-cell convection. Does  $\underline{E} = \underline{V} \times \underline{B}$  still work when there are collisions?

TODO: D, E, F layers. Stratification of different species. Ionization by UV radiation, charged particle precipitation, and cosmic rays.

TODO: Precipitation. Inverted V. Aurorae.

Table 1.1: Integrated Ionospheric Conductivity (S)

	$\Sigma_0$	$\Sigma_P$	$\Sigma_H$
Active Day	—	13.0	17.0
Quiet Day	—	5.6	10.2
Active Night	—	0.8	0.3
Quiet Night	—	0.2	0.3

## 1.2 Geomagnetic Disturbances

The quiet geomagnetic behavior described in Section 1.1 is punctuated by

### 1.2.1 Storms

### 1.2.2 Substorms

Storms! CMEs, etc.

TODO: Definition of a substorm comes from [1]. [74] added the growth phase (previously it was just expansion and recovery).

What causes a storm.

Storm effects: outer magnetosphere, inner magnetosphere, on the ground.

## 1.3 Field Line Resonance

TODO: Haven't read this paper yet, but it looks fun: [33].

TODO: Fishbone instability?

TODO: Lab Alfvén waves as LASP?

The motion of a charged particle in a dipole field can be described in terms of three fundamental motions. First is cyclotron motion: a particle orbits around a magnetic field line. Second is bounce motion: while orbiting, the particle moves along the field line like a bead on a string, back and forth between the northern and southern hemispheres<sup>5</sup>. Third is drift motion: as particles orbit and bounce, they also experience a net azimuthal motion<sup>6</sup>

TODO: Electron cyclotron frequency is on the order of  $\sim 1 \text{ MHz}$  in the ionosphere, and more like  $\sim 1 \text{ kHz}$  in the magnetosphere. Much faster than drift or bounce timescales. Ion cyclotron frequency... down by a factor of  $\frac{m_e}{\pm}$ .

TODO: Bounce timescales are faster closer to Earth (where the field lines are short) and slower further out. Something like 10 s to 100 s. Bounce timescales depend only on velocity, right?

TODO: Drift timescales vary significantly based on particle energy. Dai[16] showed a nice example of 100 keV ions drifting with a period of  $\sim 100 \text{ s}$ . Bounce and drift timescales can overlap – this turns out to be important. This doesn't depend on mass, right? Just kinetic energy.

TODO: Electromagnetic waves are oscillating all over the place in the magnetosphere. When wave oscillation frequency lines up with a particle's cyclotron, bounce, and/or drift period, there can be an ongoing energy exchange between the wave and the particle.

---

<sup>5</sup>As a particle approaches Earth, it experiences an ever-stronger magnetic field. The particle's perpendicular kinetic energy increases in proportion with the magnetic field in order to conserve its first adiabatic invariant. When the perpendicular kinetic energy can no longer increase – that is, when the parallel kinetic energy is zero – the particle bounces back. (If the parallel kinetic energy is sufficiently large, the particle doesn't bounce; it precipitates into the atmosphere.)

<sup>6</sup>Particle drift is a consequence of the gradient-curvature drift in Earth's curved, nonuniform magnetic field.

Wave-particle interaction. Analogy: a surfer moves along with a wave in the ocean, continuously gaining energy from it. Particles, by “surfing” on electromagnetic waves, can become energized as well as radially displaced. This is a significant energy transport mechanism.

TODO: Any waves with frequencies of  $10^{-3}$  Hz to 1 Hz are termed ULF waves – ultra low frequency. ULF waves are furthermore categorized in terms of their morphological characteristics. Pc waves are continuous (exhibiting a fairly consistent waveform over a large number of wave periods) while Pi are irregular; the waves are further partitioned into frequency bands. See Table 1.2.

TODO: These are Jacobs’ original ranges... but are they really reflective of the jargon still used? It’s weird that these ranges bottom out so far below 1000s.

Table 1.2: IAGA Magnetic Pulsation Frequency Bands[48]

	Pc1	Pc2	Pc3	Pc4	Pc5	Pi1	Pi2
Period (s)	0.2–5	5–10	10–45	45–150	150–600	1–40	40–150
Frequency (mHz)	200–5000	100–200	22–100	7–22	2–7	25–1000	7–25

TODO: While the IAGA characterizations are based on wave morphology, they do a decent job of deliniating between the different underlying physical processes as well. Pi2 pulsations (irregular waves with periods of a minute or two) tend to be excited on the nightside; they are associated with substorm onset (though the processes that give rise to Pi2s – and their relation to substorm onset – remains controversial). Pc1 and Pc2 pulsations tend to be EMIC (electromagnetic ion cyclotron) waves near the ion gyrofrequency, which are important for the precipitation of electrons (?).

Pi2: “Clearly linked to substorm disturbances and other impulsive dynamics are the irregularly shaped waves in the 7–25-mHz band referred to as Pi2. Recent work on these waves suggests that their periodicity reflects the spectrum of global mode excitations of the plasmasphere but there is a competing proposal that the dominant frequencies are imposed by the modulated flows in the magnetotail.”[53]

**TODO:** The present work is specifically concerned with field line resonances near the plasmapause. These waves fall in the Pc4 range, with frequencies around 10 mHz<sup>7</sup>.

The study of field line resonance dates back to Dungey's seminal work in 1954[21], which describes the possibility of an Alfvén wave bouncing back and forth along a magnetic field line.

**TODO:** Field line resonance is an important energy transport mechanism!

Drift resonance happens when the bounce frequency of an Alfvén wave between the northern and southern ionospheres matches the bounce frequency of nearby particles. It allows the energization of ring current and radiation belt particles through drift and drift-bounce resonance[24, 70, 81, 95]. By multiple wave-particle interactions, poloidal ULF waves [FLRs] can lead to radial diffusion of radiation belt particles[23, 82, 108].

**TODO:** Above the profile, Bob scales the value that's read in as  $r^5$  or something. Is there a citation for that?

The Alfvén speed is then computed per  $v_A^2 \equiv \frac{1}{\mu_0 \epsilon_{\perp}}$ .

The Alfvén speed is computed from Kelley's low-density profile, modified to take into account the local density. The density, in turn, is the sum of a plasmaspheric profile and a high-latitude auroral profile.

$$\epsilon_{\perp} = (\text{low-density tabulated value}) + \frac{n\bar{m}}{B_0^2} \quad (1.1)$$

Where  $\bar{m}$  is the ambient mean molecular mass and  $B_0$  is the zeroth-order magnetic field strength,  $B_0 = 3.11 \times 10^4 \text{ nT} \left(\frac{R_E}{r}\right)^3 \sqrt{1 + 3 \cos^2 \theta}$ . Note that  $3.11 \times 10^4 \text{ nT}$  is the value of the Earth's magnetic field at the equator on Earth's surface.

**TODO:** Does Kelley list the electric constant or the Alfvén speed?

---

<sup>7</sup>Notably, field line resonances can also fall within the Pc3 and Pc5 ranges.

### Alfvén Bounce Frequencies

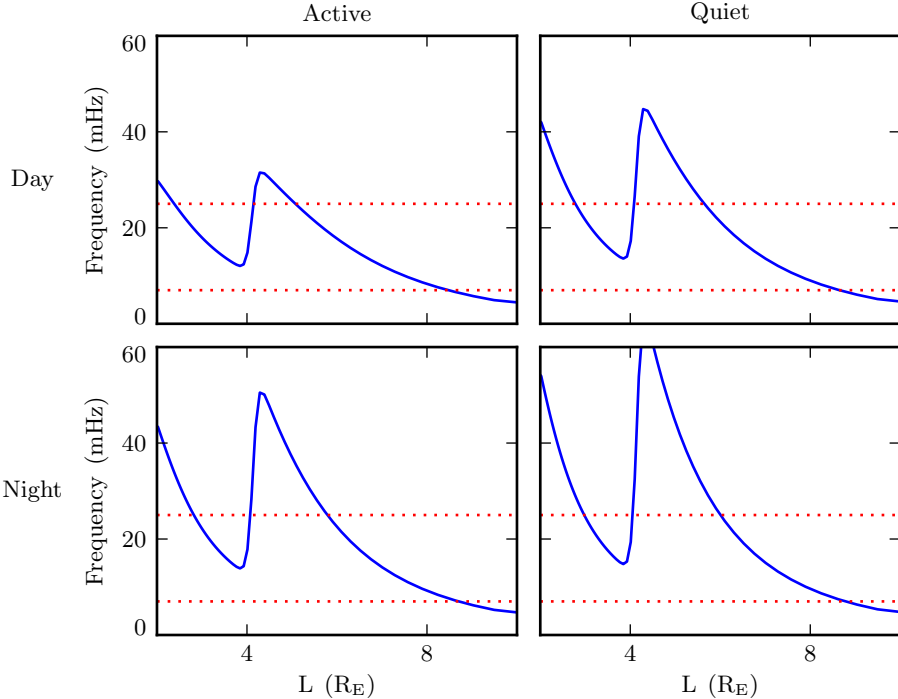


Figure 1.1: Alfvén bounce frequency profiles, computed by integrating the the Alfvén speed back and forth over a field line.  $f_A = \left[ \oint \frac{dz}{v_A} \right]^{-1}$ . Dotted lines indicate the Pc4 frequency range, 7 mHz to 25 mHz. In each profile, the effect of the plasmapause is clearly visible, centered at  $L = 4$ . Field lines just inside and just outside the plasmapause appear susceptible to resonance in the Pc4 band.

**TODO:** Talk about how the size of the plasmasphere can be adjusted, and  $4 R_E$  is just a typical value.

ULF waves have been shown to correlate with pulsating aurora and with chorus[49]. It's believed that (in the case presented) substorm injection drove Pc4-5 pulsations, which modulated chorus waves, which pitch-angle scattered electrons with energies on the order of 10 keV.

**TODO: Early observations of field line resonance.**

Ground signatures in the Pc4 range identified in the 1930s[?]. Decades later, simultaneous observations at conjugate foot points of the same field line showed FLR structure[?]. And looked at their structure (?) [?].

**TODO: Modern observations – how do we justify using a 2.5D model? Localization in MLT.**

Pc4 pulsations are radially localized, per multiple satellite observations[25], and spread no more than about 8 hours MLT. They peak around  $L$  of 5 to 6, with lower occurrence rate 2.5 to 9[3, 62].

**TODO: Radial localization.**

The plasmapause – representing a sharp change in Alfvén speed – is important for ULF waves. Waves are trapped and scattered by the effective potential well, analogous to Schrödinger’s equation[58, 59, 14]. This has been shown theoretically[54, 60, 55, 69] (most recent is [69]) and observationally[97, 98].

**TODO: On the generation of FLRs:**

Compressional waves come from the outer boundary, propagating across field lines[66].

Compressional driving doesn’t preclude drift or drift-bounce resonance[117, 118].

Plasmapause refilling may cause onset of the instability that drives noncompressional Pc4s[25, 61].

Low  $m$  is compressional[45]. Drivers may include KH at the magnetopause[9, 94, 64], variations in solar wind pressure (such as interplanetary shocks)[117, 118, 41, 17, 52], and waves in the foreshock region[91, 99].

AMPTE/CCE data has shown a correlation between poloidal Pc4 activity and intense ring current flux near the equator[27]. Poloidal Pc4s may be caused by phase space gradients[16]. Fundamental standing waves are possibly excited by drift resonance of ions with energy around 100 keV[107, 16].

“To summarize, the general buffetting of the magnetosphere by variations in the solar

wind dynamic pressure, or perhaps by sporadic magnetic reconnection, provides a broad band energy source to the magnetosphere. The magnetospheric cavity as a whole rings at its own eigenfrequencies, thus transporting energy at just those frequencies to field lines deep in the magnetosphere. Those field lines whose eigenfrequencies match one of the cavity eigenfrequencies couple to the cavity mode and resonate strongly, producing the classical field line resonance signature.[45]”

**TODO: Observational constraints for ground-based work on FLRs:**

High-modenumber ULF pulsations are damped by the ionosphere, making it more difficult to observe them on the ground[46]. Small structures are also damped; resonances narrower than  $\sim 100$  km aren’t visible on the ground. See also Glassmeier and Stellmacher, 2000 (about small latitude), and Wright and Yeoman, 1999, Yeoman and Wright, 2001 about large  $m$ .

Second harmonic poloidal waves – as most of [15]’s events are – are unlikely to cause a Pg event on the ground[105].

It’s perhaps not surprising that, finding events based on ground signatures,  $m$  would skew low. High- $m$  waves can’t penetrate the ionosphere. Multi-spacecraft observation of a ULF wave with very high modenumber (70+) and no apparent ground signature[102].

**TODO: The ionosphere is important:**

A Hall-conducting ionosphere reflects ULF waves[44].

Poloidal and toroidal ULF polarizations are treated differently by the ionosphere[38] (more recently, [29]).

**TODO: Theoretical consideration of decay vs propagation, by frequency. Lysak and Yoshikawa 2006.**

Alfvén waves with small latitudinal scale[34] or high  $m$  [113, 116] are screened by the ionosphere. Attenuation factor from [46] and [31] DID NOT PRINT PROPERLY. LOOK IT UP.

Typical magnitude is order of a few nT, and a few mV/m[102].

### 1.3.1 Structure and Jargon

**TODO: Poloidal and toroidal, fundamental mode and second harmonic... make sure this vocabulary is inescapably clear!**

Drift-wave instability[42, 35, 36] is also a possibility for exciting fundamental poloidal waves, though it requires cold plasma, so it could only happen in the plasmasphere.

Fundamental poloidal mode is drift resonance, not drift bounce[84].

Pc5 waves peak around  $L$  of 7 to 9, too far out for RBSP[3, 62]. Poloidal Pc4 pulsations are common inside and outside the plasmapause. Plasmapause peaks at 4.8–5 RE and 5.8–6RE[15].

Because the inner magnetosphere is low- $\beta$  (that is, magnetic pressure dominates thermal pressure), the strength of the compressional-poloidal coupling indicates  $m$  [45].

At high  $m$ , the poloidal mode decouples from the compressional mode[45] and becomes guided[13].

Most observed guided waves are second harmonic excited by the drift-bounce resonance[47, 93, 103]. Fundamental modes, driven by drift resonance, are rarer, but have been observed[16]. The energy of the resonant particle gives  $m$ , recall  $\omega - m\omega_d = 0$  or something[80].

A recent survey of Van Allen Probe data showed that Pc4 pulsations – the poloidal ones, at least – occur primarily during geomagnetically active times, near the plasmapause, over just a handful of hours of dayside MLT[15]. This confirmed and refined older work[26].

In the example shown of a fundamental mode poloidal Pc4, and in the example of a higher harmonic Pc4, a mishmash of toroidal activity is present. [15], figure 8 and 9 respectively.

Compressional poloidal Pc4 pulsations are much more common during storms, but not particularly sensitive to storm phase. Noncompressional ones occur primarily during recovery[15, 90, 25, 2]. Note that Dai[15] was pretty generous about what counted as a storm... anything that hits  $-30$  nT. So [75] may not have counted the same way when

they found no particular correlation with storm phase. **TODO: Fishbone instability.**  
McGuire 1983, Chen 1984. Similar phenomenon, but for lab plasmas.

An ideal poloidal mode decays to the toroidal mode in the presence of curved magnetic field lines[88] or a gradient in the Alfvén speed[71]. The time is proportional to the azimuthal wavenumber[71]. An analytical follow-up agreed with the numerical work[72].

**TODO:** Mann gives the poloidal-to-toroidal decay time to be  $\tau = \frac{d\lambda}{d\omega'_A}$ , where  $\lambda = \frac{m}{2\pi r}$  and  $\omega'_A$  is the spatial derivative of the Alfvén bounce frequency, but this doesn't seem to line up. When  $\tau$  is computed using our Alfvén bounce frequencies, the result is much less than 1 s. Double-checking is necessary.

[13]: Standing Alfvén waves in the magnetosphere. Theoretical fundamental toroidal and poloidal modes can vary by up to 30 % in frequency.

Second harmonic: Br leads Ea by 90 degrees. Fundamental mode: Br lags Ea by 90 degrees. DEPENDS ON SIGN OF MLAT. [15]

Low- $m$  waves tend to be more muddled... driven by broadband sources rather than resonance[15].

Drift resonance is the fundamental mode. Drift-bounce is higher harmonics[15].

**TODO: Do the unambiguous Pc4 events in [101] and [16] also have a mishmash of toroidal activity?**

Fundamental mode is rare. Of 390 noncompressional events, Dai identified 19 to be clearly fundamental mode and 197 to be clearly second harmonic[15].

Fast and shear (toroidal and poloidal) modes are coupled by nonzero Hall conductivity[50].

Shear mode incident on the ionosphere, pederson current closes FAC, Hall current then generates a fast mode wave which may be detected in space or on the ground[106].

Toroidal mode is usually associated with external driving[9, 94].

Guided poloidal wave arises as  $m$  goes to infinity[86].

Observations show that the poloidal mode is most excited in the second harmonic[13, 47, 4, 93, 104, 27] even when there is a strong compressional component[100, 39, 109, 92].

Theoretical justifications for why the second harmonic would be preferentially excited in the ring current environment. Basically, the drift-balloonning mode is only unstable in the case of antisymmetry[95, 10, 11, 8].

Observations of odd-mode poloidal waves... possible fundamental[114, 28].

### 1.3.2 Giant Pulsations

First Pg observation[5].

Pc4 pulsations in general tend to exhibit meridional polarization on the ground, but giant pulsations have east-west polarization[105].

Pgs are most common during solar minimum, perhaps because of decreased mass loading of heavy ions[18].

Observations in space indicate that Pgs are fundamental poloidal mode[56, 43, 57, 105, 32].

Pgs are rare[7]. Most Pgs observed on the ground have  $m$  in the range 16 to 35[105]. Motoba[75] found  $m$  values in the range 10 to 15 for a sample of Pgs. Previous studies[90, 30, 43, 84] are in general agreement that Pg modenumbers fall into the range 16 to 35.

A long-period Alfvén wave passing through the ionosphere is rotated by about 90 degrees[79, 44]. That would translate a poloidal resonance in space to an east-west ground signature.

[75] suggests that Pgs originate from the fundamental poloidal mode waves at all local times.

It seems to be the convention to find a Pg event on the ground, then look at satellite data. That's certainly what was done in [75].

Per [75], most Pg events happen around  $L = 7$ , but some do happen near the plasma-pause, as seen(?) by [36].

"The AL distribution shown in Figure 14c are consistent with the findings of [90] that Pgs occur as the magnetosphere recovers from previous activities (substorms)." [75]

Finds this to be reasonable because it's "very likely" that energetic ions injected into the inner magnetosphere from the magnetotail provide energy to Pgs.

Analysis of GOES data from 2008 to 2013 shows about 100 Pg events. They are concentrated on the morningside. No particular correlation with storm phase[75].

Recall compressional poloidal Pc4s are mostly during storm time, and noncompressional are mostly specifically during late recovery[15]. Only 19 fundamental poloidal mode examples were identified from the 390 noncompressional poloidal events.

Another past study: [104]. Satellite data is surveyed and classified by polarization, harmonic, wavenumber, etc, in order to determine the mechanisms for generating Alfvén waves. Old, but still pretty representative, according to Motoba[75].

### 1.3.3 Motivations for the Present Work

Dai writes, in his 2015 paper[15], "It is not clear why noncompressional [high- $m$ ] Pc4 poloidal waves, which are presumably driven by instability within the magnetosphere, preferentially occur on the dayside."

Motoba[75], similarly, notes "It is unclear whether other generation mechanisms of fundamental standing waves ... can explain the localization of Pgs in local time."

The present work uses a numerical model to investigate the preferential occurrence of field line resonances in the Pc4 range – particularly first-harmonic poloidal modes, such as giant pulsations – in MLT.

Giant pulsations have variously been referred to as "intriguing"[36]

"rare"[7], even to the point of being "a small subset of fundamental poloidal waves"[102] – note that it's well known that fundamental poloidal mode waves are already rare in comparison to second harmonic waves.

**TODO: What's going on with the MLT localization of Pc4 pulsations? Is there something spooky going on with the driving? Maybe the ionosphere just kills FLRs on the nightside!**

TODO: What's so special about Pgs? How rare are they, really, compared to fundamental poloidal modes in general? How does that line up with the occurrence rate of nice, sinusoidal waveforms in second-harmonic Pc4s? That is, is there something special about Pgs, or do they just live in a “sweet spot” with respect to constraints on observation and resonance?

TODO: The goal here is to clarify and unify several constraints on the viability and observability of FLRs.

# Chapter 2

# Model

TODO: The present chapter sketches the fundamental equations of waves in a cold, resistive plasma. It then illustrates the implementation of a two and a half dimensional Alfvén wave code to model those waves. Finally, takes a look at a little something extra that the code might like.

## 2.1 Dispersion Relation

Before delving into the implementation of the numerical model, it's instructive to consider the fundamental equations of waves in a cold, resistive plasma.

The evolution of electric and magnetic fields is governed by Ampère's Law and Faraday's Law. Notably, the present work takes the linearized versions of Maxwell's equations; the vectors  $\underline{E}$  and  $\underline{B}$  indicate perturbations above the zeroth-order magnetic field.

$$\underline{\epsilon} \cdot \frac{\partial}{\partial t} \underline{E} = \frac{1}{\mu_0} \nabla \times \underline{B} - \underline{J} \quad \frac{\partial}{\partial t} \underline{B} = -\nabla \times \underline{E} \quad (2.1)$$

Current follows Ohm's Law. For currents perpendicular to the background magnetic field, Kirchhoff's formulation is sufficient. Conductivity is much higher along the magnetic field lines<sup>1</sup>, so it's appropriate to also include the electron inertial term<sup>2</sup>.

$$0 = \underline{\sigma}_{\perp} \cdot \underline{E}_{\perp} - \underline{J}_{\perp} \quad \frac{1}{\nu} \frac{\partial}{\partial t} J_z = \sigma_0 E_z - J_z \quad (2.2)$$

Derivatives in Equations (2.1) and (2.2) can be evaluated by performing a Fourier transform. They can then be combined, eliminating the magnetic field and current terms.

$$\begin{aligned} 0 &= \underline{E}_{\perp} + \frac{v_A^2}{\omega^2} (\underline{k} \times \underline{k} \times \underline{E})_{\perp} + \frac{i}{\epsilon_{\perp} \omega} \underline{\sigma}_{\perp} \cdot \underline{E}_{\perp} \\ 0 &= E_z + \frac{c^2}{\omega^2} (\underline{k} \times \underline{k} \times \underline{E})_z + \frac{i\omega_P^2}{\omega(\nu - i\omega)} E_z \end{aligned} \quad (2.3)$$

The speed of light, Alfvén speed (including the displacement current correction), plasma frequency, and parallel conductivity are defined in the usual way:

$$c^2 \equiv \frac{1}{\mu_0 \epsilon_0} \quad v_A^2 \equiv \frac{1}{\mu_0 \epsilon_{\perp}} \quad \omega_P^2 \equiv \frac{ne^2}{m_e \epsilon_0} \quad \sigma_0 \equiv \frac{ne^2}{m_e \nu} \quad (2.4)$$

---

<sup>1</sup>The dipole coordinate system is defined rigorously in Section 2.2.2; at present, it's sufficient to take  $\hat{z}$  parallel to the zeroth-order magnetic field, and  $\hat{x}$  and  $\hat{y}$  perpendicular to  $\hat{z}$  (and to each other).

<sup>2</sup>Electron inertial effects are not included in the model described in Section 2.2, or in the results in Chapter 3; however, their implementation and impact are explored in Section 2.3.

Using the vector identity  $\underline{k} \times \underline{k} \times \underline{E} = \underline{k} \underline{k} \cdot \underline{E} - k^2 \underline{E}$ , Equation (2.3) can be reassembled into a single expression,

$$0 = \left( \underline{\underline{\mathbb{I}}} + \frac{1}{\omega^2} \underline{\underline{V}}^2 \cdot \underline{k} \underline{k} - \frac{k^2}{\omega^2} \underline{\underline{V}}^2 + \frac{i}{\omega} \underline{\underline{\Omega}} \right) \cdot \underline{E} \quad (2.5)$$

Where  $\underline{\underline{\mathbb{I}}}$  is the identity tensor and in  $x$ - $y$ - $z$  coordinates<sup>3</sup>,

$$\underline{\underline{V}}^2 \equiv \begin{bmatrix} v_A^2 & 0 & 0 \\ 0 & v_A^2 & 0 \\ 0 & 0 & c^2 \end{bmatrix} \quad \text{and} \quad \underline{\underline{\Omega}} \equiv \begin{bmatrix} \frac{\sigma_P}{\epsilon_{\perp}} & \frac{-\sigma_H}{\epsilon_{\perp}} & 0 \\ \frac{\sigma_H}{\epsilon_{\perp}} & \frac{\sigma_P}{\epsilon_{\perp}} & 0 \\ 0 & 0 & \frac{\omega_P^2}{(\nu - i\omega)} \end{bmatrix} \quad (2.6)$$

In Equation (2.5), the expression in parentheses is the dispersion tensor. Nontrivial solutions exist only when its determinant is zero. This gives rise to a seventh-order polynomial in  $\omega$ , so rather than a direct solution it's necessary to consider limits of specific interest.

**TODO:** Without loss of generality, the wave vector  $\underline{k}$  may be taken to lie in the  $x$ - $z$  plane – that is, with  $k_y = 0$ . The distinction between the two perpendicular directions is discussed in Section 2.1.4.

### 2.1.1 Guided Propagation

The wave vector of a field line resonance aligns closely to the background magnetic field. By supposing that the two align exactly (that is, taking  $k_x = 0$ ), the parallel and perpendicular components of the dispersion relation are decoupled.

The parallel-polarized component is quadratic, and thus can be solved directly.

$$0 = \omega^2 + i\nu\omega - \omega_P^2 \quad \text{so} \quad \omega = -\frac{i\nu}{2} \pm \sqrt{\omega_P^2 - \frac{\nu^2}{4}} \quad (2.7)$$

It bears noting that the plasma frequency is large – not just compared to Pc4 frequencies,

---

<sup>3</sup>Note that the present definition of  $\underline{\underline{\Omega}}$  differs slightly from that used in Section 2.2.4.

but even compared to the collision frequencies in the ionosphere<sup>4</sup>.

Expanding Equation (2.7) with respect to large  $\omega_P$ , the dispersion relation becomes

$$\omega^2 = \omega_P^2 \pm i\nu\omega_P + \dots \quad (2.8)$$

Equation (2.8) can hardly be called a wave, as it does not depend on the wave vector  $\underline{k}$ . Rather, it is the plasma oscillation<sup>5</sup>: electrons vibrating in response to a charge separation along the background magnetic field.

The plasma oscillation is of little interest to the study of field line resonance. The two phenomena are separated by six orders of magnitude in frequency. Nevertheless, the topic is revisited in Section 2.3.

The perpendicular components of the dispersion relation give an expression quartic in  $\omega$ .

$$0 = \omega^4 + 2i\frac{\sigma_P}{\epsilon_\perp}\omega^3 - \left(2k_z^2v_A^2 + \frac{\sigma_P^2 + \sigma_H^2}{\epsilon_\perp^2}\right)\omega^2 - 2ik_z^2v_A^2\frac{\sigma_P}{\epsilon_\perp}\omega + k_z^4v_A^4 \quad (2.9)$$

Like the parallel-polarized component above, Equation (2.9) can be solved directly. Noting that  $\pm$  and  $\oplus$  are independent,

$$\omega = \left(\frac{\pm\sigma_H - i\sigma_P}{2\epsilon_\perp}\right) \oplus \sqrt{k_z^2v_A^2 + \left(\frac{\pm\sigma_H - i\sigma_P}{2\epsilon_\perp}\right)^2} \quad (2.10)$$

Also like the parallel-polarized component, the exact solution is less useful than its Taylor expansion. The Pedersen and Hall conductivities are large near the ionospheric boundary, but fall off quickly; for the vast majority of the field line, the ratios  $\frac{\sigma_P}{\epsilon_\perp}$  and  $\frac{\sigma_H}{\epsilon_\perp}$  are small compared to field line resonance frequencies. Expanding with respect to

---

<sup>4</sup>The collision frequency may match or exceed the plasma frequency for a thin slice at the bottom of the ionosphere, where the density of neutral atoms is large; however, it falls off quickly. Above an altitude of 200 km, conservatively[78], the plasma frequency exceeds the collision frequency by an order of magnitude or more.

<sup>5</sup>The plasma oscillation is also called the Langmuir wave, after Irving Langmuir.

small conductivity gives

$$\omega^2 = k_z^2 v_A^2 \oplus k_z v_A \frac{\sigma_H \pm i\sigma_P}{\epsilon_{\perp}} + \dots \quad (2.11)$$

This is the Alfvén wave, with a shift to its frequency due to the conductivity of the ionosphere. It travels along the background magnetic field like a bead on a string, with electric and magnetic field perturbations perpendicular to the magnetic field line (and to one another).

**TODO:** Jesse calls this the magnetosonic wave, and uses “Alfvén wave” for the other one!

### 2.1.2 Compressional Propagation

**TODO:** Is it fair to say “compressional” to mean “perpendicular” in terms of propagation? It would be nice to have different jargon for the propagation directions and the polarization directions.

The partner to guided motion is compressional motion; in order for energy to move across field lines, the wave vector must have a component perpendicular to  $\hat{z}$ . If the wave vector is completely perpendicular to the magnetic field line ( $k_z = 0$ ), the parallel and perpendicular components of the dispersion relation decouple, as in Section 2.1.1.

The parallel-polarized component of the dispersion relation is

$$0 = \omega^3 + i\nu\omega^2 - (k_x^2 c^2 + \omega_P^2) \omega - ik_x^2 c^2 \nu \quad (2.12)$$

Equation (2.12) can be solved directly, though its solution (as a cubic) is far too long to be useful. Expanding with respect to the large plasma frequency, gives

$$\omega^2 = k^2 c^2 + \omega_P^2 - i\nu\omega_P + \dots \quad (2.13)$$

This is the O mode, a compressional wave with an electric field perturbation along the background magnetic field. Like the plasma oscillation discussed in Section 2.1.1, its

frequency is very large compared to that of a field line resonance.

The perpendicular-polarized component of the compressional dispersion relation is also cubic.

$$0 = \omega^3 + 2i\frac{\sigma_P}{\epsilon_\perp}\omega^2 - \left(2k_x^2v_A^2 + \frac{\sigma_P^2 + \sigma_H^2}{\epsilon_\perp^2}\right)\omega - ik_x^2v_A^2\frac{\sigma_P}{\epsilon_\perp} \quad (2.14)$$

A wave moving across magnetic field lines near the ionospheric boundary will encounter large  $\frac{\sigma_P}{\epsilon_\perp}$  and  $\frac{\sigma_H}{\epsilon_\perp}$ , while at moderate to high altitudes those ratios will be small. Solving Equation (2.14) in those two limits respectively gives:

$$\omega^2 = k_x^2v_A^2 \pm ik_xv_A\frac{\sigma_P}{\epsilon_\perp} + \dots \quad \text{and} \quad \omega^2 = k_x^2v_A^2 + \left(\frac{\sigma_H \pm i\sigma_P}{\epsilon_\perp}\right)^2 + \dots \quad (2.15)$$

**TODO:** These expressions are both the same sort of wave, obviously, with shifts in frequency due to the ionospheric conductivity. Double check terminology; is it still an Alfvén wave if it's propagating across magnetic field lines, or does a different name become more correct? Electric field perturbation is still perpendicular to the background magnetic field.

### 2.1.3 High Altitude Limit

In the limit of large radial distance, it's reasonable to take the collision frequency to zero; doing so also neglects the Pedersen and Hall conductivities.

Whereas in Sections 2.1.1 and 2.1.2 it was the parallel-polarized component of the dispersion relation that factored out from the other two, the high altitude limit decouples the component polarized out of the  $x$ - $z$  plane. The  $\hat{y}$ -polarized dispersion relation is simply:

$$\omega^2 = k^2v_A^2 \quad (2.16)$$

This solution is analogous to Equations (2.11) and (2.15). The electric field perturbation is perpendicular to both the background magnetic field and the wave vector (though

those two evidently need not be perpendicular to one another).

The other two components of the high altitude dispersion tensor give an expression quadratic in  $\omega^2$ :

$$0 = \omega^4 - (k_x^2 c^2 + k_z^2 v_A^2 + \omega_P^2) \omega^2 + k_z^2 v_A^2 \omega_P^2 \quad (2.17)$$

Which can be solved for

$$\omega^2 = \frac{1}{2} (k_x^2 c^2 + k_z^2 v_A^2 + \omega_P^2) \pm \sqrt{\frac{1}{4} (k_x^2 c^2 + k_z^2 v_A^2 + \omega_P^2)^2 - k_z^2 v_A^2 \omega_P^2} \quad (2.18)$$

Noting again that  $\omega_P$  is very large, the two roots can be expanded to

$$\omega^2 = k_z^2 v_A^2 \left( 1 + \frac{k_x^2 c^2 + k_z^2 v_A^2}{\omega_P^2} \right) + \dots \quad \text{and} \quad \omega^2 = k_x^2 c^2 + k_z^2 v_A^2 + \omega_P^2 + \dots \quad (2.19)$$

**TODO:** The first part looks like an Alfvén wave. The second is faster than the plasma frequency, so we don't really care about it.

#### 2.1.4 Implications to the Present Work

The present section's findings carry three significant implications for the present work.

First – with the exception of the plasma oscillation, which is revisited in Section 2.3 – waves are expected to propagate at the Alfvén speed. This, in combination with the grid configuration, will constrain the time step that can be used to model them numerically. The time step must be sufficiently small that information traveling at the Alfvén speed cannot “skip over” entire grid cells<sup>6</sup>

Second, the results of the present section allow an estimate of the magnitude of parallel electric field that might be expected from a field line resonance compared to its perpendicular electric field. Between the full dispersion tensor form in Equation (2.5) and the

---

<sup>6</sup>As is the convention, the time step is scaled down from the smallest Alfvén zone crossing time by a Courant factor, typically 0.1, meaning that it takes at least ten time steps to cross a grid cell.

Alfvén wave described by Equation (2.19),

$$\left| \frac{E_z}{E_x} \right| = \frac{k_x k_z c^2}{\omega^2 - k_x^2 c^2 - \omega_P^2} \sim \frac{k^2 c^2}{\omega_P^2} \quad (2.20)$$

In essence, the relative magnitudes of the parallel and perpendicular electric fields should be in proportion to the square of the relative magnitudes of the electron inertial length (1 km to 100 km, depending on altitude) and the wavelength ( $\sim 10^5$  km). That is, parallel electric fields should be smaller than the perpendicular electric fields by six or more orders of magnitude.

Finally, the dispersion relations shown above indicate how the behavior of a field line resonance should behave as the azimuthal modenumber becomes large.

Whereas the shear Alfvén wave's dispersion relation depends only on the parallel component of the wave vector, the compressional Alfvén wave depends on its magnitude:  $\omega^2 = k^2 v_A^2$ . If the frequency is smaller than  $k v_A$ , the wave will become evanescent. The wave vector's magnitude can be no smaller than its smallest component, however, and the azimuthal component scales with the azimuthal modenumber:  $k_y \sim \frac{2\pi m}{r}$ .

This imposes a frequency cutoff on compressional Alfvén waves which scales with the azimuthal modenumber. At small values of  $m$ , most of the magnetosphere is conducive to compressional Alfvén waves in the Pc4 frequency range. As  $m$  increases, and the wave vector with it, the inner magnetosphere becomes increasingly inaccessible to them.

TODO: Create this figure, obviously. Plot for  $m$  of 1, 8, 64 (arranged horizontally). Log scale in mHz. Title “Compressional Alfvén Cutoff Frequency”

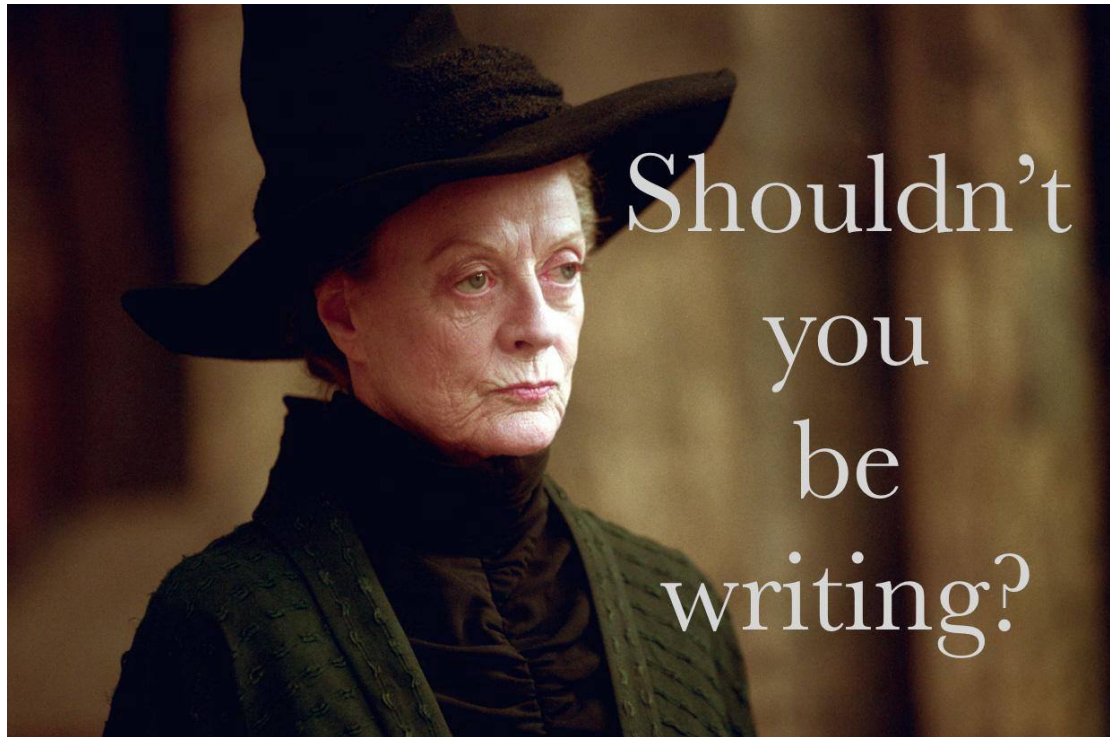


Figure 2.1: Using the Alfvén speed profile described in Section 2.2.1, and taking  $k_y \sim \frac{2\pi m}{r}$  as a lower bound for the magnitude of the wave vector, the above figure demonstrates the lowest frequency at which compressional Alfvén waves may propagate as a function of position and  $m$ .

## 2.2 “Tuna Half” Dimensional Simulation

The present section describes the implementation of Tuna, a new two and a half dimensional Alfvén wave code based largely on work by Lysak[65, 68].

The half-integer dimensionality refers to the fact that Tuna’s spatial grid resolves a two-dimensional slice of the magnetosphere, but that electric and magnetic fields – as well as their curls – are three-dimensional vectors. This apparent contradiction is reconciled by the use of a fixed azimuthal modenumber,  $m$ . Electric and magnetic fields are taken to be complex-valued, varying azimuthally per  $\exp(im\phi)$ ; derivatives with respect to  $\phi$  are then replaced by a factor of  $im$ .

Unlike a fully three-dimensional code, Tuna cannot resolve the evolution of wave structures in the azimuthal direction. Furthermore, the model does not allow coupling between the dayside and nightside magnetospheres. What Tuna does offer is efficiency. The model’s economical geometry allows it to include a realistic Earthward boundary: grid spacing on the order of 10 km, a height-resolved ionospheric conductivity tensor, and even the computation of magnetic field signatures at the ground. Such features are computationally infeasible for a large global code.

Tuna was developed with field line resonance in mind. As discussed in Section 1.3, such waves are azimuthally localized, minimizing the importance of Tuna’s missing half dimension. Moreover, because field line resonances are known to be affected by both the ionosphere and the plasmasphere, a faithful treatment of the inner magnetosphere is a crucial part of studying them numerically.

Perhaps the most exciting feature of Tuna is its novel driving mechanism: ring current perturbation. Codes similar to Tuna have traditionally been driven using compressional pulses at the outer boundary[65, 68, 112, 111]. This has precluded the investigation of waves with large azimuthal modenumber – such as giant pulsations – which are guided, and thus must be driven from within the magnetosphere.

TODO: The support software – the driver and the plotter – are also significant. Do they get mentioned here? Does the Git repository where the code can be accessed get mentioned here?

### 2.2.1 Physical Parameter Profiles

Tuna models Earth's magnetic field to be an ideal dipole:

$$\underline{B}_0 = 3.1 \times 10^4 \text{ nT} \left( \frac{R_E}{r} \right)^3 \left( 2 \cos \theta \hat{r} - \sin \theta \hat{\theta} \right) \quad (2.21)$$

Number density is taken to be the sum of an inverse-radial-dependent auroral profile and a plasmaspheric profile dependent on the  $L$ -shell[68].

$$n = n_{AZ} \frac{r_{AZ}}{r} + n_{PS} \exp\left(\frac{-L}{L_{PS}}\right) \left( \frac{1}{2} - \frac{1}{2} \tanh \frac{L - L_{PP}}{\delta L_{PP}} \right) \quad (2.22)$$

Where typical values are  $n_{AZ} = 10 / \text{cm}^3$  (the number density at the base of the auroral zone),  $r_{AZ} = 1 R_E$  (the scale height of the auroral density distribution),  $n_{PS} = 10^4 / \text{cm}^3$  (the number density at the base of the plasmasphere),  $L_{PS} = 1.1 R_E$  (the scale  $L$  of the plasmasphere),  $L_{PP} = 4$  (the  $L$  value of the plasmapause), and  $\delta L_{PP} = 0.1$  (the thickness of the plasmapause, in  $L$ ).

The perpendicular component of the electric tensor,  $\epsilon_{\perp}$ , is computed based on Kelley's[51] tabulated low-density values,  $\epsilon_K$ , which are adjusted to take into account the effects of high density in the plasmapause.

$$\epsilon_{\perp} = \epsilon_K + \frac{Mn}{B_0^2} \quad (2.23)$$

Where  $M$  is the mean molecular mass, which is large ( $\sim 28 \text{ u}$ ) at 100 km altitude, then drops quickly (down to 1 u by  $\sim 1000 \text{ km}$ )[68].

The Alfvén speed profile is computed from the perpendicular electric constant in the usual way,  $v_A^2 \equiv \frac{1}{\mu_0 \epsilon_{\perp}}$ . This form takes into account the effect of the displacement current, which becomes important in regions where the Alfvén speed approaches the speed of light.

While the density profile is held constant for all runs discussed in the present work, the Alfvén speed profile is not. Four different for the low-density perpendicular electric

constant  $\epsilon_K$ , corresponding to the differing ionospheric conditions between the dayside and the nightside, and between the high and low points in the solar cycle. These differences are visible in Figure 2.2, particularly in the size of the ionospheric Alfvén resonator (the peak in Alfvén speed in the high-latitude ionosphere).

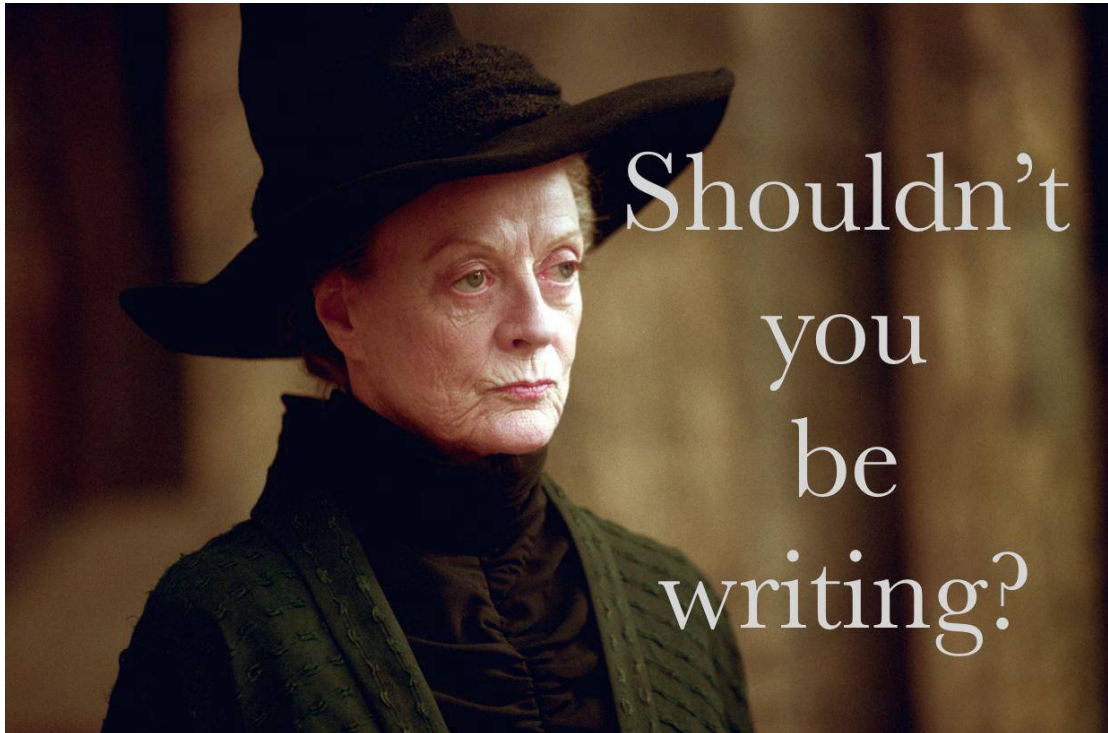


Figure 2.2: Alfvén speed profiles are based on low-density values tabulated by Kelley[51]. They are adjusted to take into account the density of the plasmapause and mass loading near the Earthward boundary.

Ionospheric conductivity profiles are also based on values tabulated by Kelley, adjusted by Lysak[68] to take into account the abundance of heavy ions near the Earthward boundary. Pedersen, Hall, and parallel conductivities are each resolved by altitude, as shown in Figure 2.3.

Tuna's physical parameter profiles are static over the course of each run. Even so-called ultra low frequency waves like Pc4 pulsations are fast compared to convective timescales in the magnetosphere.

Pedersen (Blue), Hall (Red), and Parallel (Green) Conductivities

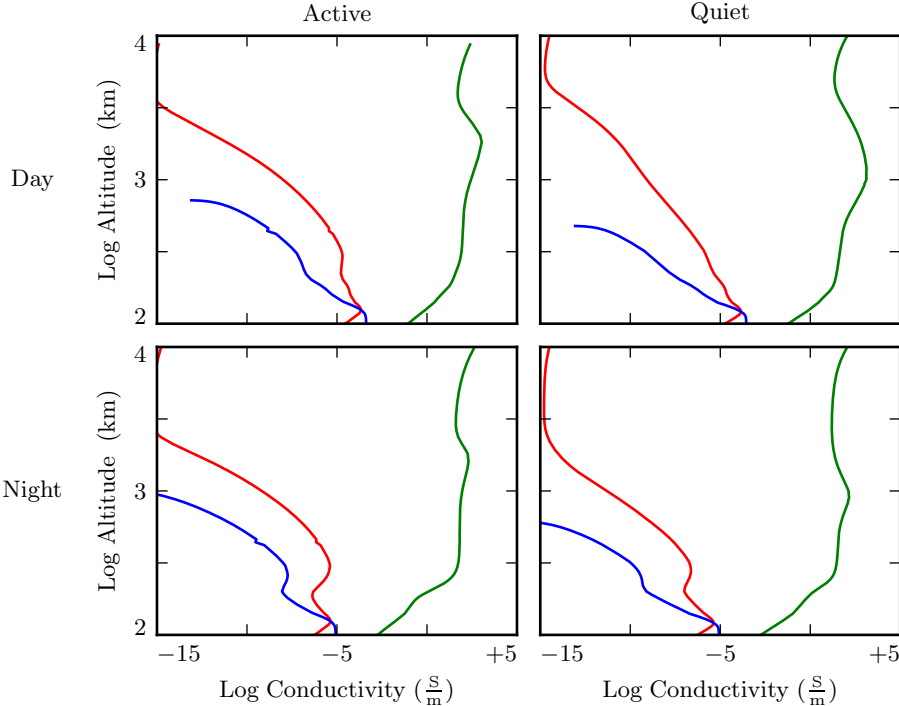


Figure 2.3: Ionospheric conductivity profiles are adapted by Lysak[68] from Kelley's tabulated values[51]. These profiles allow Tuna to simulate magnetosphere-ionosphere coupling under a variety of conditions.

## 2.2.2 Coordinate System

Field line resonance has traditionally been modeled by straightening the field lines into a rectangular configuration[21, 71], by unrolling the azimuthal coordinate into a cylindrical coordinate system[88], or through the use of dipole coordinates[87]<sup>7</sup>:

$$x \equiv -\frac{\sin^2 \theta}{r} \quad y \equiv \phi \quad z \equiv \frac{\cos \theta}{r^2} \quad (2.24)$$

Where  $r$ ,  $\theta$ , and  $\phi$  take on their usual spherical meanings of radial distance, colatitude,

---

<sup>7</sup>The dipole coordinates  $x$ ,  $y$  and  $z$  are perhaps more commonly named  $\mu$ ,  $\phi$ , and  $\nu$  respectively; however, in the present work,  $\mu$  and  $\nu$  take other meanings.

and azimuthal angle respectively.

The dipole coordinate  $x$  is constant over each equipotential shell<sup>8</sup>,  $y$  is azimuthal angle, and  $z$  indexes each field line from south to north. The unit vectors  $\hat{x}$ ,  $\hat{y}$ , and  $\hat{z}$  point in the crosswise<sup>9</sup> (radially outward at the equator), azimuthal (eastward), and parallel (northward at the equator) directions respectively.

Notably, the dipole coordinates in Equation (2.24) are normal to one another. While mathematically convenient, they do not readily accommodate a fixed-altitude boundary at the ionosphere, nor do they allow the dipole magnetic field to intersect the boundary at an oblique angle, as Earth's field does. As a solution, a nonorthogonal set of dipole coordinates was developed numerically by Proehl[85], then formalized analytically by Lysak[65] in terms of their contravariant components:

$$u^1 = -\frac{R_I}{r} \sin^2 \theta \quad u^2 = \phi \quad u^3 = \frac{R_I^2}{r^2} \frac{\cos \theta}{\cos \theta_0} \quad (2.25)$$

Above,  $R_I$  is the position of the ionosphere relative to Earth's center; it's typically taken to be  $1 R_E + 100 \text{ km}$ .

Like the dipole coordinates  $x$ ,  $y$ , and  $z$ , Lysak's coordinates  $u^1$ ,  $u^2$ , and  $u^3$  correspond to  $L$ -shell, azimuthal angle, and position along a field line respectively. However, compared to  $z$ ,  $u^3$  has been renormalized using the invariant colatitude<sup>10</sup>  $\theta_0$ . As a result,  $u^3$  takes the value  $+1$  at the northern ionospheric boundary and  $-1$  at the southern ionospheric boundary for all field lines.

---

<sup>8</sup>In fact,  $x$  is inversely proportional to the McIlwain parameter.

<sup>9</sup>In the context of in situ measurements taken near the equatorial plane,  $\hat{x}$  is referred to as the radial direction; however, the present work extends the dipole grid to low altitudes, where  $\hat{x}$  can be more horizontal than vertical. The term "crosswise" is meant to indicate that  $\hat{x}$  is defined by the cross product of  $\hat{y}$  and  $\hat{z}$ .

<sup>10</sup>The invariant colatitude is the colatitude  $\theta$  at which a field line intersects the ionosphere. It is related to the McIlwain parameter by  $\cos \theta_0 \equiv \sqrt{1 - \frac{R_I}{L}}$ .

Because Lysak's coordinate system is not orthogonal<sup>11</sup>, it's necessary to consider covariant and contravariant basis vectors separately.

$$\hat{e}_i \equiv \frac{\partial}{\partial u^i} \underline{r} \quad \hat{e}^i \equiv \frac{\partial}{\partial \underline{r}} u^i \quad (2.26)$$

Covariant basis vectors  $\hat{e}_i$  are normal to the curve defined by constant  $u^i$ , while contravariant basis vectors  $\hat{e}^i$  are tangent to the coordinate curve (equivalently,  $\hat{e}^i$  is normal to the plane defined by constant  $u^j$  for all  $j \neq i$ ). These vectors are reciprocal<sup>12</sup> to one another, and can be combined to give components of the metric tensor  $\underline{\underline{g}}$ [19].

$$\hat{e}^i \cdot \hat{e}_j = \delta_j^i \quad g_{ij} \equiv \hat{e}_i \cdot \hat{e}_j \quad g^{ij} \equiv \hat{e}^i \cdot \hat{e}^j \quad (2.27)$$

The metric tensor allows rotation between covariant and contravariant representations of vectors.

$$A_i = g_{ij} A^j \quad \text{and} \quad A^i = g^{ij} A_j \quad \text{where} \quad A_i \equiv \underline{A} \cdot \hat{e}_i \quad \text{and} \quad A^i \equiv \underline{A} \cdot \hat{e}^i \quad (2.28)$$

In addition, the determinant of the metric tensor is used to define cross products and curls<sup>13</sup>.

$$(\underline{A} \times \underline{B})^i = \frac{\varepsilon^{ijk}}{\sqrt{g}} A_j B_k \quad \text{and} \quad (\nabla \times \underline{A})^i = \frac{\varepsilon^{ijk}}{\sqrt{g}} \frac{\partial}{\partial u^j} A_k \quad \text{where} \quad g \equiv \det \underline{\underline{g}} \quad (2.29)$$

Explicit forms of the basis vectors and metric tensor can be found in the appendix of Lysak's 2004 paper[65]. At present, it's sufficient to note the mapping between Lysak's

---

<sup>11</sup>Curves of constant  $u^1$  and curves of constant  $u^3$  can intersect at non-right angles.

<sup>12</sup>The symbol  $\delta_j^i$  is the Kronecker delta; the present work also makes use of the Levi-Civita symbol  $\varepsilon^{ijk}$  and Einstein's convention of implied summation over repeated indeces[22].

<sup>13</sup>The square root of the determinant of the metric tensor is called the Jacobian. It's sometimes denoted using the letter  $J$ , which the present work reserves for current.

basis vectors and the usual dipole unit vectors<sup>14</sup>.

$$\hat{x} = \frac{1}{\sqrt{g^{11}}} \hat{e}^1 \quad \hat{y} = \frac{1}{\sqrt{g^{22}}} \hat{e}^2 \quad \hat{z} = \frac{1}{\sqrt{g^{33}}} \hat{e}_3 \quad (2.30)$$

The basis vectors can also be mapped to the spherical unit vectors, though Equation (2.31) is valid only at the ionospheric boundary.

$$\hat{\theta} = \frac{1}{\sqrt{g_{11}}} \hat{e}_1 \quad \hat{\phi} = \frac{1}{\sqrt{g_{22}}} \hat{e}_2 \quad \hat{r} = \frac{1}{\sqrt{g_{33}}} \hat{e}^3 \quad (2.31)$$

The coordinates converge at the equatorial ionosphere, so an inner boundary is necessary to maintain finite grid spacing. It's typically placed at  $L = 2$ . The outer boundary is at  $L = 10$ . The dipole approximation of Earth's magnetic field is tenuous at the outer boundary (particularly on the dayside); however, in practice, wave activity is localized inside  $L \sim 7$ . The grid is spaced uniformly in  $u^1$ , which gives finer resolution close to Earth and coarser resolution at large distances.

Spacing in  $u^3$  is set by placing grid points along the outermost field line. The points are closest together at the ionosphere, and grow towards the equator. The spacing increases in a geometric fashion, typically by 3%.

Typically, Tuna uses a grid 150 points in  $u^1$  by 350 points in  $u^3$ . The result is a resolution on the order of 10 km at the ionosphere, which increases to the order of 10<sup>3</sup> km at the midpoint of the outermost field line.

There are no grid points in  $u^2$  due to the two-and-a-half-dimensional nature of the model. Fields are assumed to vary as  $\exp(imu^2)$ , so derivatives with respect to  $u^2$  are equivalent to a factor of  $im$ . In effect, this means that the real component of each field is azimuthally in phase with the (purely real) driving, while imaginary values represent behavior that is azimuthally offset.

The simulation's time step is set based on the grid spacing. As is the convention,  $\delta t$  is set to match the smallest Alfvén zone crossing time, scaled down by a Courant factor

---

<sup>14</sup>TODO: Do these need to be written out? Referring people to the code, which will be in a public Git repository, is also a possibility.

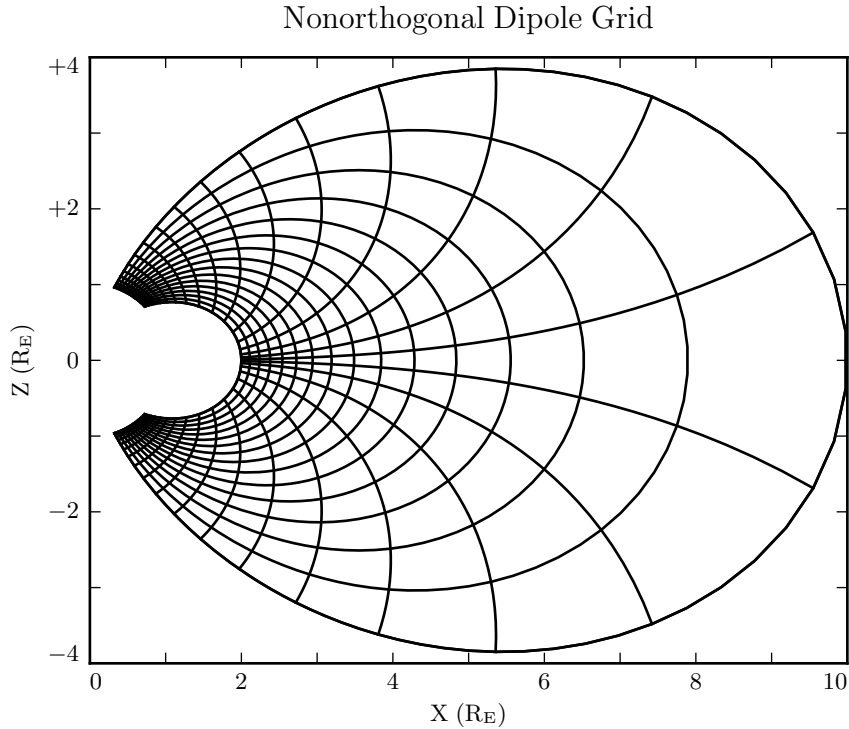


Figure 2.4: The model’s nonorthogonal dipole grid. Every fifth point is shown in each direction. The high concentration of grid points near Earth’s equator is a consequence of the coordinate system, which converges at the equatorial ionosphere.

(typically 0.1). It bears noting that the smallest crossing time need not correspond to the smallest zone; the Alfvén speed peaks several thousand kilometers above Earth’s surface, in the so-called Ionospheric Alfvén Resonator[68]. A typical time step is on the order of  $10^{-5}$  s.

### 2.2.3 Driving

Models similar to Tuna have traditionally been driven using compression at the outer boundary[65, 68, 112, 111]. Such driving can be envisioned as a proxy for solar wind compression, Kelvin-Helmholtz effects at the magnetopause, and so on. However, because

of the constraints imposed by the dispersion relation for Alfvén waves<sup>15</sup>, simulations driven from the outer boundary are constrained to the consideration of waves with low azimuthal modenumber (equivalently, large azimuthal wavelength).

This issue is demonstrated in Figure 2.5. At low modenumber, energy delivered at the outer boundary is able to propagate across field lines in order to stimulate resonances in the inner magnetosphere. However, as modenumber increases, Alfvén waves become increasingly guided, and the inner magnetosphere is unaffected by perturbations at the outer boundary.

In order to simulate high-modenumber Alfvén waves in the inner magnetosphere – such as giant pulsations – a new driving mechanism is necessary. Perturbation of the ring current is a natural choice, as Alfvén waves in the Pc4 range are known to interact with ring current particles through drift and drift-bounce resonances. The ring current is a dynamic region, particularly during and after geomagnetic storms; it’s easy to imagine the formation of localized inhomogeneities.

In order to estimate an appropriate magnitude for perturbations of the ring current, the Sym-H storm index is used. The index is measured once per minute, and so cannot directly detect ring current modulations in the Pc4 frequency range. Instead, the index is transformed into the frequency domain, allowing a fit of its pink noise<sup>16</sup>.

As shown in Figure 2.6, a Fourier transform of the Sym-H index (taken here from the June 2013 storm) suggests that magnetic field perturbations at Earth’s surface due to ring current activity in the Pc4 frequency range could be up to the order of  $10^{-2}$  nT. Supposing that the ring current is centered around  $5 R_E$  geocentric, that corresponds to a current on the order of 0.1 MA. Tuna’s driving is spread using a Gaussian profile in  $u^1$  (typically centered at  $L = 5$ ) and  $u^3$  (typically centered just off the equator), with a characteristic area of  $1 R_E^2$ ; this gives a current density on the order of  $10^{-4} \mu\text{A}/\text{m}^2$ .

**TODO:** Admittedly, estimating the strength of localized perturbations using Sym-H – an index averaged over the entire globe – is a bit of a kludge.

---

<sup>15</sup>See Section 2.1.4.

<sup>16</sup>Pink noise, also called  $\frac{1}{f}$  noise, refers to the power law decay present in the Fourier transforms of all manner of physical signals.

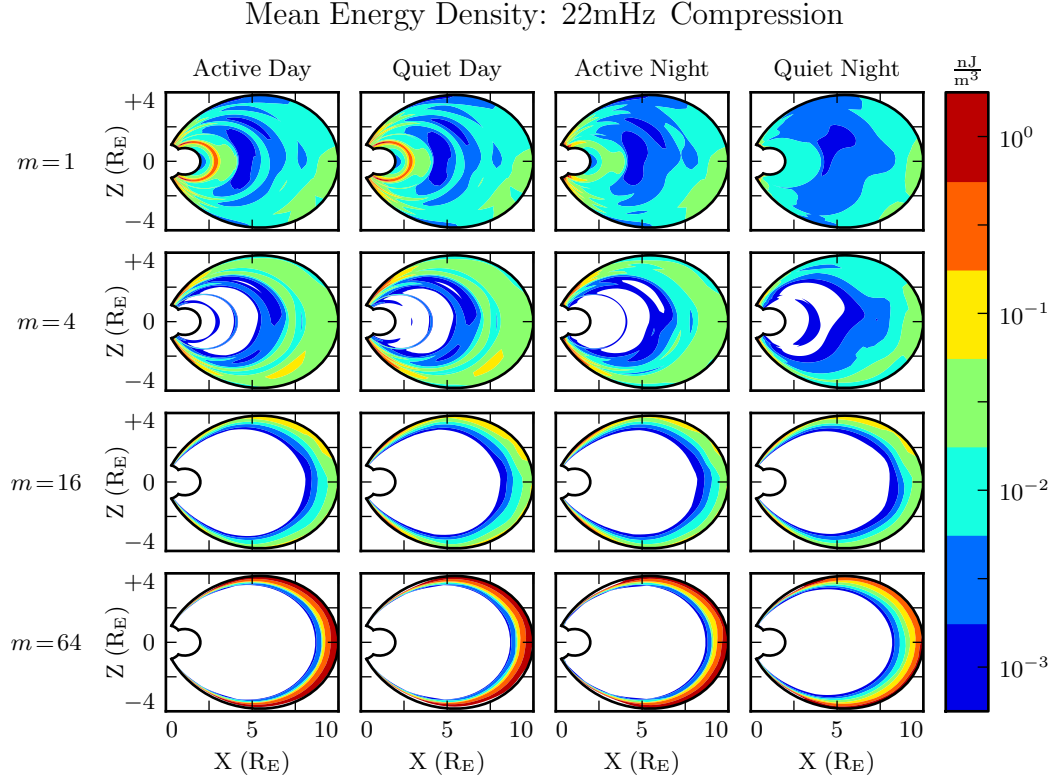


Figure 2.5: Each cell presents the mean energy density over the course of a 300s run, as a function of position, due to compressional driving at the outer boundary. Azimuthal modenumber varies by row, and ionospheric conditions vary by column. For runs with small azimuthal modenumber, it's clear that energy is able to propagate across field lines and stimulate wave activity in the inner magnetosphere. When the modenumber is large, energy is unable to penetrate to the inner magnetosphere. Notably, the large values on the bottom row should be taken with a grain of salt; it's not clear that the model's results are reliable when waves are continuously forced against the boundary.

In situ observations of Pc4 pulsations and giant pulsations have shown waves with modenumbers across the range  $1 \lesssim m \lesssim 100$ [16, 15, 102]. Simulations are carried out across that range, corresponding to ring current perturbations with azimuthal extent as small as  $0.5 R_E$ .

**TODO:** Driving is sinusoidal.

**TODO:** In case it's not clear: Chapter 3 discusses ONLY simulations using ring current

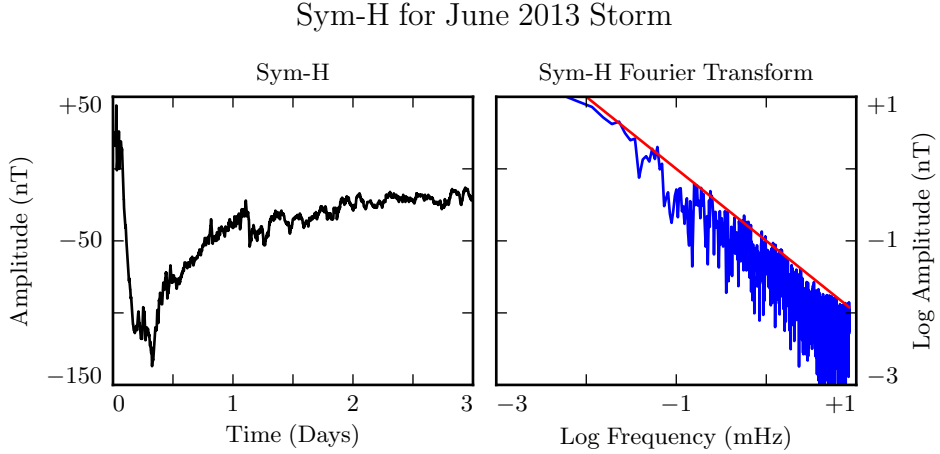


Figure 2.6: The Sym-H storm index[76] measures magnetic perturbations on Earth’s surface due to ring current activity. The amplitude of oscillations in the Pc4 range is estimated by fitting the pink noise in its Fourier transform.

driving. The only compressional driving we look at is Figure 2.5.

#### 2.2.4 Maxwell’s Equations

Tuna simulates the evolution of electromagnetic waves in accordance with Ampère’s Law and Faraday’s Law. Computation is carried out on a Yee grid[115]: electric fields and magnetic fields are offset by half a time step, and each field component is defined on either odd or even grid points in each dimension to ensure that curls are computed using centered differences.

The Ohmic current in Ampère’s Law is replaced with  $\underline{\sigma} \cdot \underline{E}$  per Kirchhoff’s formulation of Ohm’s Law. Then, taking  $\underline{J}$  to represent the driving current discussed in Section 2.2.3, Maxwell’s equations can be written

$$\frac{\partial}{\partial t} \underline{B} = -\nabla \times \underline{E} \quad \underline{\epsilon} \cdot \frac{\partial}{\partial t} \underline{E} = \frac{1}{\mu_0} \nabla \times \underline{B} - \underline{J} - \underline{\sigma} \cdot \underline{E} \quad (2.32)$$

It is convenient to introduce shorthand for the curl of each field:  $\underline{C} \equiv \nabla \times \underline{E}$  and

$\underline{F} \equiv \nabla \times \underline{B} - \mu_0 \underline{J}$ . Or, recalling Equation (2.29),

$$C^i = \frac{\varepsilon^{ijk}}{\sqrt{g}} \frac{\partial}{\partial u^j} E_k \quad F^i = \frac{\varepsilon^{ijk}}{\sqrt{g}} \frac{\partial}{\partial u^j} B_k - J^i \quad (2.33)$$

In these terms, Faraday's Law can simply be written:

$$\frac{\partial}{\partial t} B^i = -C^i \quad (2.34)$$

Writing each component out explicitly, and using the metric tensor (per Equation (2.28)) to eliminate contravariant magnetic field components<sup>17</sup>, Equation (2.34) becomes:

$$\begin{aligned} B_1 &\leftarrow B_1 - g_{11} \delta t C^1 - g_{13} \delta t C^3 \\ B_2 &\leftarrow B_2 - g_{22} \delta t C^2 \\ B_3 &\leftarrow B_3 - g_{31} \delta t C^1 - g_{33} \delta t C^3 \end{aligned} \quad (2.35)$$

Note that the  $\leftarrow$  operator is used in Equation (2.35) to indicate assignment, rather than equality. Terms on the left are new, while those on the right are old.

Unlike Faraday's Law, Ampère's Law cannot be trivially solved. Not only does the derivative of  $\underline{E}$  depend on its own future value, but the crosswise and azimuthal components of the equation are coupled by the Hall terms in the conductivity tensor. Fortunately, the electric tensor can be inverted, allowing a solution by integrating factors:

$$\underline{\underline{\epsilon}} \cdot \frac{\partial}{\partial t} \underline{E} = \frac{1}{\mu_0} \underline{F} - \underline{\underline{\sigma}} \cdot \underline{E} \quad \text{becomes} \quad \left( \underline{\underline{\Omega}} + \underline{\underline{\epsilon}} \frac{\partial}{\partial t} \right) \cdot \underline{E} = \underline{\underline{V}}^2 \cdot \underline{F} \quad (2.36)$$

---

<sup>17</sup>Fields are stored only in terms of their covariant components, and curls in terms of their contravariant components. This reduces Tuna's memory footprint (since each field need not be stored twice) as well as its computational cost (since time need not be spent rotating between bases). As a result, Tuna's solutions to Maxwell's equations are linear expressions whose coefficients are a mishmash of physical constants and geometric factors. To save time, each coefficient is computed once and stored, rather than being multiplied out from scratch with each time step.

Where  $\underline{\underline{\mathbb{I}}}$  is the identity tensor and in  $x$ - $y$ - $z$  coordinates<sup>18</sup>,

$$\underline{\underline{V}^2} \equiv \frac{1}{\mu_0} \underline{\underline{\epsilon}}^{-1} = \begin{bmatrix} v_A^2 & 0 & 0 \\ 0 & v_A^2 & 0 \\ 0 & 0 & c^2 \end{bmatrix} \quad \text{and} \quad \underline{\underline{\Omega}} \equiv \underline{\underline{\epsilon}}^{-1} \cdot \underline{\underline{\sigma}} = \begin{bmatrix} \frac{\sigma_P}{\epsilon_{\perp}} & \frac{-\sigma_H}{\epsilon_{\perp}} & 0 \\ \frac{\sigma_H}{\epsilon_{\perp}} & \frac{\sigma_P}{\epsilon_{\perp}} & 0 \\ 0 & 0 & \frac{\sigma_0}{\epsilon_0} \end{bmatrix} \quad (2.37)$$

Multiplying through by  $\exp(\underline{\underline{\Omega}} t)$  and applying the product rule, Equation (2.36) becomes<sup>19</sup>

$$\frac{\partial}{\partial t} \left( \exp(\underline{\underline{\Omega}} t) \cdot \underline{\underline{E}} \right) = \exp(\underline{\underline{\Omega}} t) \cdot \underline{\underline{V}^2} \cdot \underline{\underline{F}} \quad (2.38)$$

Equation (2.38) can then be integrated over a small time step  $\delta t$  and expressed in terms of the assignment operator introduced in Equation (2.34).

$$\underline{\underline{E}} \leftarrow \exp(-\underline{\underline{\Omega}} \delta t) \cdot \underline{\underline{E}} + \delta t \exp(-\underline{\underline{\Omega}} \frac{\delta t}{2}) \cdot \underline{\underline{V}^2} \cdot \underline{\underline{F}} \quad (2.39)$$

The tensor exponential can be evaluated by splitting  $\underline{\underline{\Omega}}$  into the sum of its diagonal and Hall components<sup>20</sup>. The Hall exponential condenses into sines and cosines, giving a rotation around the magnetic field line.

$$\underline{\underline{E}} \leftarrow \exp(-\underline{\underline{\Omega}}' \delta t) \cdot \underline{\underline{R}}_z \left( \frac{-\sigma_H \delta t}{\epsilon_{\perp}} \right) \cdot \underline{\underline{E}} + \delta t \underline{\underline{V}^2} \cdot \exp(-\underline{\underline{\Omega}}' \frac{\delta t}{2}) \cdot \underline{\underline{R}}_z \left( \frac{-\sigma_H \delta t}{2\epsilon_{\perp}} \right) \cdot \underline{\underline{F}} \quad (2.40)$$

Where

$$\underline{\underline{R}}_z(\theta) = \begin{bmatrix} \cos \theta & -\sin \theta & 0 \\ \sin \theta & \cos \theta & 0 \\ 0 & 0 & 1 \end{bmatrix} \quad \text{and} \quad \underline{\underline{\Omega}}' \equiv \begin{bmatrix} \frac{\sigma_P}{\epsilon_{\perp}} & 0 & 0 \\ 0 & \frac{\sigma_P}{\epsilon_{\perp}} & 0 \\ 0 & 0 & \frac{\sigma_0}{\epsilon_0} \end{bmatrix} \quad (2.41)$$

---

<sup>18</sup>Note the parallel component of the present definition of  $\underline{\underline{\Omega}}$  differs slightly from that used in Section 2.1.

<sup>19</sup>Tensor exponentiation is analogous to scalar exponentiation[40]:  $\exp(\underline{\underline{T}}) \equiv \sum_n \frac{1}{n!} \underline{\underline{T}}^n$ .

<sup>20</sup>For tensors,  $\exp(\underline{\underline{S}} + \underline{\underline{T}}) = \exp(\underline{\underline{S}}) \exp(\underline{\underline{T}})$  as long as  $\underline{\underline{S}} \cdot \underline{\underline{T}} = \underline{\underline{T}} \cdot \underline{\underline{S}}$ .

The parallel component of term of Equation (2.40) is simply

$$E_z \leftarrow E_z \exp\left(\frac{-\sigma_0 \delta t}{\epsilon_0}\right) + c^2 \delta t F_z \exp\left(\frac{-\sigma_0 \delta t}{2\epsilon_0}\right) \quad (2.42)$$

Or, using Equation (2.30) to map to the covariant basis,

$$E_3 \leftarrow E_3 \exp\left(\frac{-\sigma_0 \delta t}{\epsilon_0}\right) + c^2 \delta t (g_{31} F^1 + g_{33} F^3) \exp\left(\frac{-\sigma_0 \delta t}{2\epsilon_0}\right) \quad (2.43)$$

Tuna's conductivity profile gives a minimum value of  $\frac{\sigma_0 \delta t}{\epsilon_0}$  on the order of  $10^3$ , making  $\exp\left(\frac{-\sigma_0 \delta t}{\epsilon_0}\right)$  far too small to be stored in a double precision variable<sup>21</sup>. That is, this model takes  $E_3$  (and, proportionally,  $E_z$ ) to be uniformly zero. This issue is revisited in Section 2.3.

The perpendicular components of Equation (2.40) give the expressions:

$$\begin{aligned} E_1 + \frac{g^{13}}{g^{11}} E_3 &\leftarrow E_1 \cos\left(\frac{-\sigma_H \delta t}{\epsilon_\perp}\right) \exp\left(\frac{-\sigma_P \delta t}{\epsilon_\perp}\right) \\ &+ E_2 \sin\left(\frac{-\sigma_H \delta t}{\epsilon_\perp}\right) \exp\left(\frac{-\sigma_P \delta t}{\epsilon_\perp}\right) \sqrt{\frac{g^{22}}{g^{11}}} \\ &+ E_3 \cos\left(\frac{-\sigma_H \delta t}{\epsilon_\perp}\right) \exp\left(\frac{-\sigma_P \delta t}{\epsilon_\perp}\right) \frac{g^{13}}{g^{11}} \\ &+ F^1 \cos\left(\frac{-\sigma_H \delta t}{2\epsilon_\perp}\right) \exp\left(\frac{-\sigma_P \delta t}{2\epsilon_\perp}\right) \frac{v_A^2 \delta t}{g^{11}} \\ &+ F^2 \sin\left(\frac{-\sigma_H \delta t}{2\epsilon_\perp}\right) \exp\left(\frac{-\sigma_P \delta t}{2\epsilon_\perp}\right) \frac{v_A^2 \delta t}{\sqrt{g^{11} g^{22}}} \end{aligned} \quad (2.44)$$

---

<sup>21</sup>Not coincidentally,  $\frac{\sigma_0}{\epsilon_0}$  can also be written  $\frac{\omega_P^2}{\nu}$ . At the ionosphere, the collision frequency  $\nu$  is fast compared to field line resonance timescales, but it's still slow compared to the plasma frequency.

and

$$\begin{aligned}
E_2 \leftarrow & -E_1 \sin\left(\frac{-\sigma_H \delta t}{\epsilon_{\perp}}\right) \exp\left(\frac{-\sigma_P \delta t}{\epsilon_{\perp}}\right) \sqrt{\frac{g^{11}}{g^{22}}} \\
& + E_2 \cos\left(\frac{-\sigma_H \delta t}{\epsilon_{\perp}}\right) \exp\left(\frac{-\sigma_P \delta t}{\epsilon_{\perp}}\right) \\
& - E_3 \sin\left(\frac{-\sigma_H \delta t}{\epsilon_{\perp}}\right) \exp\left(\frac{-\sigma_P \delta t}{\epsilon_{\perp}}\right) \frac{g^{13}}{\sqrt{g^{11} g^{22}}} \\
& - F^1 \sin\left(\frac{-\sigma_H \delta t}{2\epsilon_{\perp}}\right) \exp\left(\frac{-\sigma_P \delta t}{2\epsilon_{\perp}}\right) \frac{v_A^2 \delta t}{\sqrt{g^{11} g^{22}}} \\
& + F^2 \cos\left(\frac{-\sigma_H \delta t}{2\epsilon_{\perp}}\right) \exp\left(\frac{-\sigma_P \delta t}{2\epsilon_{\perp}}\right) \frac{v_A^2 \delta t}{g^{22}}
\end{aligned} \tag{2.45}$$

The  $E_3$  terms in Equations (2.44) and (2.45) can be ignored at present. They are revisited in Section 2.3.

### 2.2.5 Boundary Conditions

Dirichlet and Neumann boundary conditions are applied to the electric field components and magnetic field components respectively. That is, electric fields are forced to go to zero at the inner and outer boundaries, and magnetic fields are forced to have a zero derivative normal to the inner and outer boundaries.

These boundary conditions can in principle cause nonphysical reflections at the boundary<sup>22</sup>. However, in practice, wave activity is concentrated well within the simulation domain. Simulation results are robust under an exchange of Dirichlet and Neumann boundary conditions (though a self-inconsistent set of boundary conditions, such as applying Neumann boundary conditions to  $B_1$  but Dirichlet boundary conditions to  $B_3$ , quickly causes instability).

The Earthward boundary conditions are as follows.

Between the top of the neutral atmosphere and the bottom of the ionosphere, the model includes a thin, horizontal current sheet representing the ionosphere's  $E$  layer[65]. By

---

<sup>22</sup>See, for example, the bottom row of Figure 2.5.

integrating Ampère's Law over the layer, it can be shown[29] that the horizontal electric field values at the edge of the grid are determined by the jump in the horizontal magnetic fields:

$$\underline{\underline{\Sigma}} \cdot \underline{E} = \frac{1}{\mu_0} \lim_{\delta r \rightarrow 0} \left[ \hat{r} \times \underline{B} \right]_{R_I - \delta r}^{R_I + \delta r} \quad (2.46)$$

The integrated conductivity tensor  $\underline{\underline{\Sigma}}$  can be written in  $\theta$ - $\phi$  coordinates as[65]:

$$\underline{\underline{\Sigma}} \equiv \begin{bmatrix} \frac{\Sigma_0 \Sigma_P}{\Sigma_0 \cos^2 \alpha + \Sigma_P \sin^2 \alpha} & \frac{-\Sigma_0 \Sigma_H}{\Sigma_0 \cos^2 \alpha + \Sigma_P \sin^2 \alpha} \\ \frac{\Sigma_0 \Sigma_H}{\Sigma_0 \cos^2 \alpha + \Sigma_P \sin^2 \alpha} & \Sigma_P + \frac{\Sigma_H^2 \sin^2 \alpha}{\Sigma_0 \cos^2 \alpha + \Sigma_P \sin^2 \alpha} \end{bmatrix} \quad (2.47)$$

Where  $\alpha$  is the angle between the magnetic field and the vertical direction, given by  $\cos \alpha \equiv \frac{-2 \cos \theta}{\sqrt{1+3 \cos^2 \theta}}$ , and  $\Sigma_P$ ,  $\Sigma_H$ , and  $\Sigma_0$  are the height-integrated Pedersen, Hall, and parallel conductivities respectively. Their values are determined by integrating Kelley's[51] conductivity profiles from Earth's surface to the ionospheric boundary; values are shown in Table 2.1.

Table 2.1: Integrated Atmospheric Conductivity (S)

	$\Sigma_0$	$\Sigma_P$	$\Sigma_H$
Active Day	424	0.65	6.03
Quiet Day	284	0.44	4.02
Active Night	9	0.01	0.12
Quiet Night	9	0.01	0.12

An expression for the horizontal electric fields at the boundary can be obtained by inverting Equation (2.46). After mapping to covariant coordinates per Equation (2.31),

and taking  $\Sigma \equiv \det \underline{\Sigma}$ ,

$$\begin{aligned} E_1 &\leftarrow \frac{1}{\mu_0 \Sigma} \lim_{\delta r \rightarrow 0} \left[ -\Sigma_{\theta\phi} B_1 - \sqrt{\frac{g_{11}}{g_{22}}} \Sigma_{\phi\phi} B_2 \Big|_{R_I-\delta r}^{R_I+\delta r} \right] \\ E_2 &\leftarrow \frac{1}{\mu_0 \Sigma} \lim_{\delta r \rightarrow 0} \left[ \sqrt{\frac{g_{22}}{g_{11}}} \Sigma_{\theta\theta} B_1 + \Sigma_{\phi\theta} B_2 \Big|_{R_I-\delta r}^{R_I+\delta r} \right] \end{aligned} \quad (2.48)$$

The atmospheric magnetic field is computed as a linear combination of harmonics. The neutral atmosphere is considered to be a perfect insulator, giving  $\nabla \times \underline{B} = 0$ . Combined with  $\nabla \cdot \underline{B} = 0$  (per Maxwell's equations), this allows the computation of a magnetic scalar potential  $\Psi$  such that  $\underline{B} = \nabla \Psi$  and  $\Psi$  satisfies Laplace's equation,  $\nabla^2 \Psi = 0$ .

Laplace's equation can be solved analytically; however, a numerical solution is preferable to ensure orthonormality on a discrete and incomplete<sup>23</sup> grid. After separating out the radial and azimuthal dependence in the usual way, the latitudinal component of Laplace's equation can be written in terms of  $s \equiv -\sin^2 \theta$ :

$$(4s^2 + 4s) \frac{d^2}{ds^2} Y_\ell + (4 + 6s) \frac{d}{ds} Y_\ell - \frac{m^2}{s} Y_\ell = \ell (\ell + 1) Y_\ell \quad (2.49)$$

Using centered differences to linearize the derivatives, Equation (2.49) becomes a system of coupled linear equations, one per field line. It can be solved numerically for eigenvalues  $\ell$  ( $\ell + 1$ ) and eigenfunctions  $Y_\ell$ <sup>24</sup>. In terms of the harmonics  $Y_\ell$ ,  $\Psi$  between the Earth's surface and the top of the atmosphere can be written

$$\Psi = \sum_\ell \left( a_\ell r^\ell + b_\ell r^{-\ell-1} \right) Y_\ell \quad (2.50)$$

As a boundary condition for  $\Psi$ , Earth is assumed to be a perfect conductor. This forces the magnetic field at Earth's surface to be horizontal; that is,  $B_r = \frac{\partial}{\partial r} \Psi = 0$ . Noting that solutions to Laplace's equation are orthonormal, each element of the sum

---

<sup>23</sup>As discussed in Section 2.2.2, the grid is constrained to finite  $L$ , which excludes the equator as well as the poles.

<sup>24</sup>Solving Laplace's equation analytically results in spherical harmonics indexed by both  $\ell$  and  $m$ , the separation constants for  $\theta$  and  $\phi$  respectively. In two and a half dimensions,  $\phi$  is not explicitly resolved, so  $m$  is set manually.

in Equation (2.50) must be independently zero at  $R_E$ . This allows the coefficients  $a_\ell$  and  $b_\ell$  to be expressed in terms of one another.

$$b_\ell = \frac{\ell}{\ell + 1} R_E^{2\ell+1} a_\ell \quad (2.51)$$

The current sheet at the top of the atmosphere is assumed to be horizontal, so the radial component of the magnetic field must be the same just above and just below it. Taking the radial derivative of Equation (2.50) at the top of the atmosphere, and eliminating  $b_\ell$  with Equation (2.51), gives

$$B_r = \sum_\ell \ell a_\ell R_I^{\ell-1} \left(1 - \lambda^{2\ell+1}\right) Y_\ell \quad \text{where} \quad \lambda \equiv \frac{R_E}{R_I} \sim 0.975 \quad (2.52)$$

The summation can be collapsed by “integrating” over a harmonic<sup>25</sup>. Inverse harmonics can be obtained by inverting the eigenvector matrix. Then  $Y_\ell \cdot Y_{\ell'}^{-1} = \delta_{\ell\ell'}$  by construction.

$$a_\ell = \frac{1}{\ell R_I^{\ell-1}} \frac{B_r \cdot Y_\ell^{-1}}{1 - \lambda^{2\ell+1}} \quad (2.53)$$

Combining Equations (2.50), (2.51), and (2.53) allows the expression of  $\Psi$  at the top and bottom of the atmosphere as a linear combination of radial magnetic field components at the bottom of the ionosphere.

$$\begin{aligned} \Psi_E &= \sum_\ell Y_\ell \frac{R_I}{\ell(\ell-1)} \frac{(2\ell-1)\lambda^\ell}{1-\lambda^{2\ell+1}} B_r \cdot Y_\ell^{-1} \\ \Psi_I &= \sum_\ell Y_\ell \frac{R_I}{\ell(\ell-1)} \frac{(\ell-1)+\ell\lambda^{2\ell+1}}{1-\lambda^{2\ell+1}} B_r \cdot Y_\ell^{-1} \end{aligned} \quad (2.54)$$

---

<sup>25</sup>Because the functions are defined on a discrete grid, their inner product is not an integral, but a sum:  
 $B_r \cdot Y_\ell^{-1} \equiv \sum_i B_r[i] Y_\ell^{-1}[i]$ .

Horizontal magnetic fields are obtained by taking derivatives of  $\Psi$ .

$$B_1 = \frac{\partial}{\partial u^1} \Psi \quad B_2 = \frac{\partial}{\partial u^2} \Psi \quad (2.55)$$

Horizontal magnetic field values at the top of the atmosphere are used to impose boundary conditions on the electric fields at the bottom of the ionosphere, per Equation (2.48). Those at Earth's surface are valuable because they allow a direct comparison between model output and ground magnetometer data, after being mapped to physical coordinates per Equation (2.31).

## 2.3 Electron Inertial Effects

As laid out in Section 2.2, Tuna resolves neither parallel currents nor parallel electric fields. This limits the model’s applicability to **TODO: direct acceleration of particles? double layers? Alfvénic aurorae?** and other topics closely related to field line resonance.

Parallel currents and electric fields can be added to Tuna through the consideration of electron inertial effects in Ohm’s Law:

$$0 = \sigma_0 E_z - J_z \quad \text{becomes} \quad \frac{1}{\nu} \frac{\partial}{\partial t} J_z = \sigma_0 E_z - J_z \quad (2.56)$$

With the addition of the electron inertial term, it is necessary to track the parallel current independent of the parallel electric field<sup>26</sup>. Solving by integrating factors<sup>27</sup> gives

$$J_3 \leftarrow J_3 \exp(-\nu \delta t) + \delta t \frac{ne^2}{m_e} E_3 \exp\left(-\nu \frac{\delta t}{2}\right) \quad (2.57)$$

From there, the parallel electric field can be updated directly; Equation (2.43) is replaced by the following:

$$E_3 \leftarrow E_3 + c^2 \delta t (g_{31} F^1 + g_{33} F^3) - \frac{\delta t}{\epsilon_0} J_3 \quad (2.58)$$

The present section explores the complications that arise from the addition of the electron inertial term to Ohm’s Law, as well as a few results that may be gleaned despite those complications. Notably – for reasons discussed in Section 2.3.3 – the results presented in Chapter 3 do not make use of the electron inertial term.

---

<sup>26</sup>The parallel current  $J_z$  is defined on the same points of the Yee grid as  $E_z$ . It is offset in time by half of a time step.

<sup>27</sup>The integrating factors technique is laid out explicitly for Ampère’s Law in Section 2.2.4.

### 2.3.1 The Boris Factor

With the addition of the electron inertial term, a cyclical dependence appears between Ampère's Law and Ohm's Law:

$$\frac{\partial}{\partial t} E_z \sim -\frac{1}{\epsilon_0} J_z \quad \text{and} \quad \frac{\partial}{\partial t} J_z \sim \frac{n e^2}{m_e} E_z \quad \text{so} \quad \frac{\partial^2}{\partial t^2} E_z \sim -\omega_P^2 E_z \quad (2.59)$$

That is, electron inertial effects come hand in hand with the plasma oscillation.

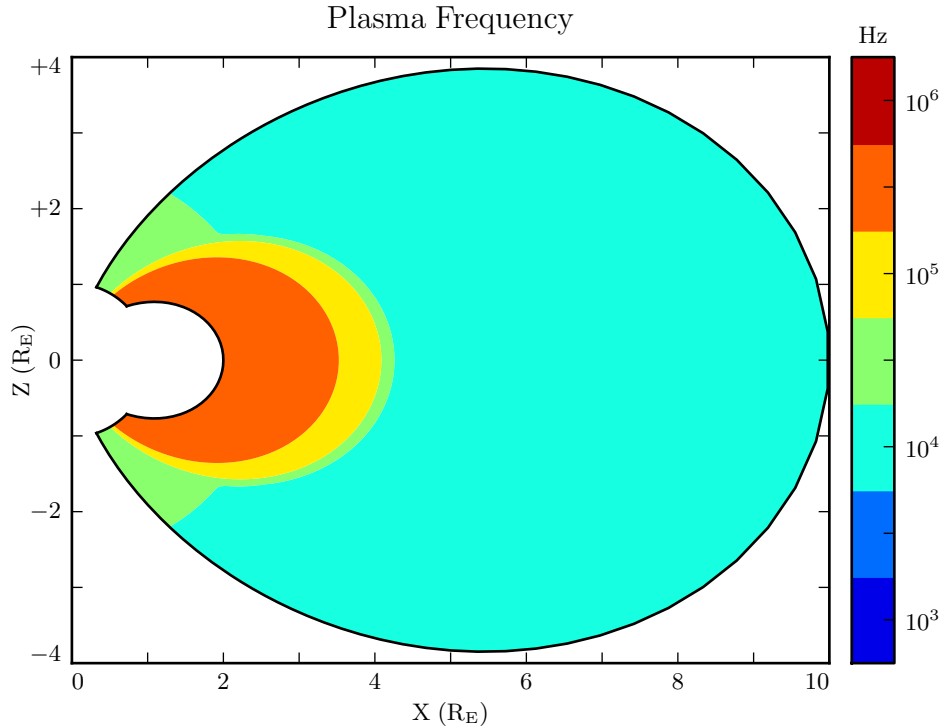


Figure 2.7: The plasma frequency reaches a peak value just under  $10^6$  Hz near the equator. Outside the plasmasphere, its value is closer to  $10^4$  Hz, which is still not well-resolved by Tuna's usual time step.

As mentioned in Section 2.1 and shown in Figure 2.7, plasma oscillation is quite fast – several orders of magnitude smaller than Tuna's time step as determined in Section 2.2.2 ( $\sim 10 \mu\text{s}$ ). This poses a conundrum. At Tuna's usual time step, the plasma oscillation

becomes unstable within seconds<sup>28</sup>. On the other hand, reducing the time step by three orders of magnitude to resolve the plasma oscillation is computationally infeasible; a run slated for an hour would require six weeks to complete.

As it happens, this problem can be solved by artificially increasing the parallel electric constant above its usual value of  $\epsilon_0$ . Doing so lowers both the speed of light and the plasma frequency within the simulation.

This technique – and others like it – has been widespread in numerical modeling since it was presented by Boris in 1970[6]. More recently, Lysak and Song considered its use specifically for the case of electron inertial effects[67]. The following paraphrases their argument.

Supposing that the current and electric field are oscillating at frequency  $\omega$ , the parallel components of Ampère's Law and Ohm's Law can be written

$$-i\omega\epsilon_0 E_z = \frac{1}{\mu_0} (\nabla \times \underline{B})_z - J_z \quad -\frac{i\omega}{\nu} J_z = \sigma_0 E_z - J_z \quad (2.60)$$

Then, eliminating the current, the parallel electric field can be related to the curl of the magnetic field by<sup>29</sup>

$$\left(1 - \frac{\omega^2 - i\nu\omega}{\omega_P^2}\right) E_z = \frac{c^2}{\omega_P^2} (\nu - i\omega) (\nabla \times \underline{B})_z \quad (2.61)$$

In Equation (2.61),  $\frac{c}{\omega_P}$  is the electron inertial length. While the speed of light and the plasma frequency each depend on  $\epsilon_0$ , their ratio does not. This allows an estimation of how much the model should be affected by an artificially-large electric constant (and thus an artificially-small plasma frequency): so long as  $\frac{\omega^2 - i\nu\omega}{\omega_P^2}$  remains small compared to unity, the model should behave faithfully.

For waves with periods of a minute or so, even perhaps-implausibly large Boris factors are allowed; for example, increasing  $\epsilon_0$  by a factor of  $10^6$  gives  $\left|\frac{\omega^2 + i\omega\nu}{\omega_P^2}\right| \lesssim 0.01$ .

---

<sup>28</sup>TODO: The plasma oscillation is unstable at large time steps because of overcorrection. For stability,  $\omega_P\delta t < 1$  is necessary.

<sup>29</sup>From Equation (2.4),  $c^2 \equiv \frac{1}{\mu_0\epsilon_0}$  and  $\sigma_0 \equiv \frac{ne^2}{m_e\nu}$  and  $\omega_P^2 \equiv \frac{ne^2}{m_e\epsilon_0}$ .

### 2.3.2 Parallel Currents and Electric Fields

As discussed in Section 2.1.4, parallel electric fields in this regime are expected to be six or more orders of magnitude smaller than the perpendicular electric fields. Numerical results show general agreement: in Figure 2.8, the parallel electric field appears comparable to its perpendicular counterparts only after its been scaled up by six orders of magnitude.



Figure 2.8: Parallel electric fields are smaller than perpendicular electric fields by about six orders of magnitude. As a result, parallel electric fields do not contribute significantly to  $\nabla \times \underline{E}$  in Faraday's Law.

As such, the inclusion of electron inertial effects does not appreciably impact the simulation's gross behavior; in Faraday's Law,  $\nabla \times \underline{E}$  is essentially unaffected. Side by side snapshots of the magnetic fields in runs carried out with and without electron inertial effects are not visibly distinguishable<sup>30</sup>

---

<sup>30</sup>In a sense, this is reassuring. It ensures that the present section does not cast doubt on the results

Even if there is no significant feedback through Faraday’s Law, it’s informative to consider the structures that arise in parallel currents and electric fields driven by perturbations in the ring current.

For example, the parallel electric field is at its maximum value in the ionosphere. This makes its structure qualitatively resemble the Poynting flux than the perpendicular electric field components.

It is furthermore notable that the parallel electric field (and the parallel current that comes from it) exhibits real and imaginary components of comparable magnitude.

As mentioned in Section 2.2, each field’s real component gives its behavior in the meridional plane where the (real) driving is delivered, while imaginary components are representative of waves offset in the azimuthal direction. The Hall conductivity in the ionosphere muddles this relationship somewhat by directly coupling the perpendicular electric field components to one another; even so, the poloidal field components ( $B_x$ ,  $E_y$ , and  $B_z$ ) are overwhelmingly real while toroidal components ( $E_x$  and  $B_y$ ) are overwhelmingly imaginary.

The parallel electric field and current defy this pattern. The real current scales more or less proportionally with the poloidal Poynting flux, and its imaginary component scales comparably with the toroidal Poynting flux. Rather than being preferentially coupled to one mode or the other, parallel currents seem to arise wherever energy is moving along the background magnetic field.

It bears noting further that the Poynting flux waveforms are rectified – they primarily carry energy Earthward. The current, on the other hand, alternates between upward and downward flow. This effect presumably arises because the current is a linear quantity while the Poynting flux is quadratic: the electric and magnetic fields that make it up oscillate in phase, so their product is positive even when they are negative.

It’s also possible to consider the effect of parallel currents and electric fields on the

---

presented in Chapter 3, where electron inertial effects are neglected.

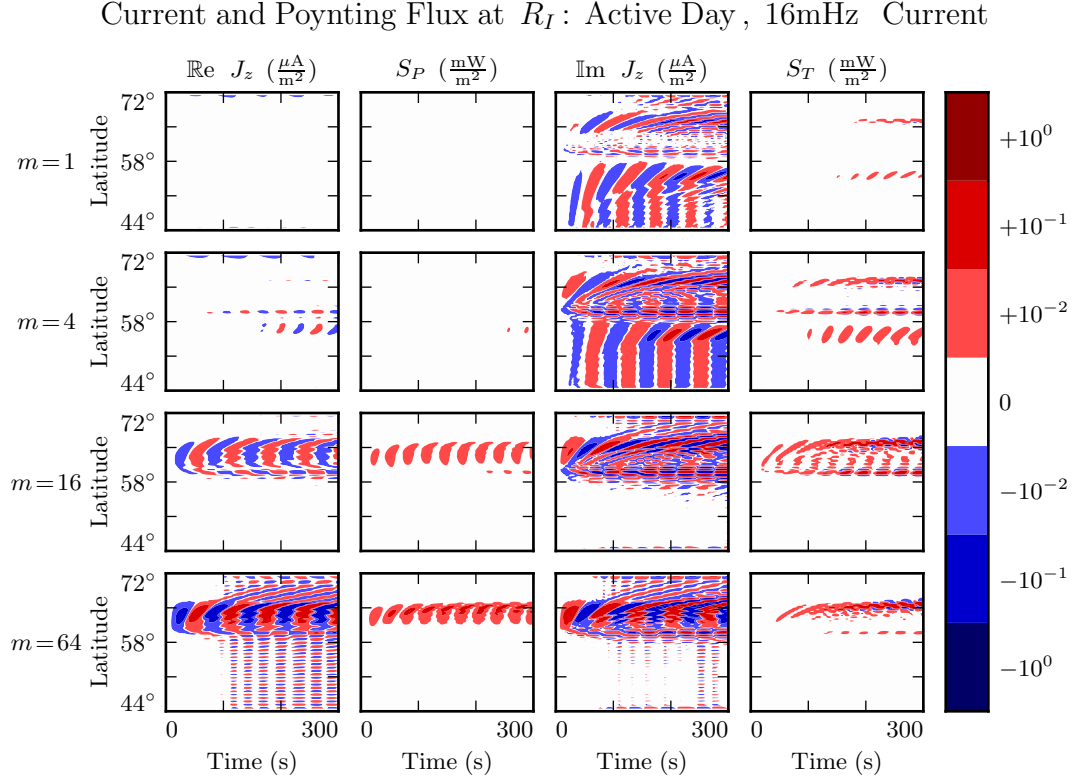


Figure 2.9: **TODO:** Perhaps unsurprisingly, field-aligned current structures at the ionospheric boundary line up with Poynting flux structures. The imaginary component of the current lines up with the toroidal Poynting flux (which is the product of imaginary  $E_x$  and imaginary  $B_y$ ), while the real current lines up with the poloidal Poynting flux ( $E_y$  and  $B_x$  are real).

ionosphere's energy budget, per Poynting's theorem:

$$-\frac{\partial}{\partial t} u = \nabla \cdot \underline{E} + \underline{J} \cdot \underline{E} \quad (2.62)$$

As shown in Figure 2.10, little energy transfer in the ionosphere is mediated by perpendicular components of the Poynting flux. The parallel component of  $\underline{J} \cdot \underline{E}$  is comparably unimportant. The energy deposited in the ionosphere by the Poynting flux matches closely with the energy lost to Joule dissipation – as it should, to conserve energy – but

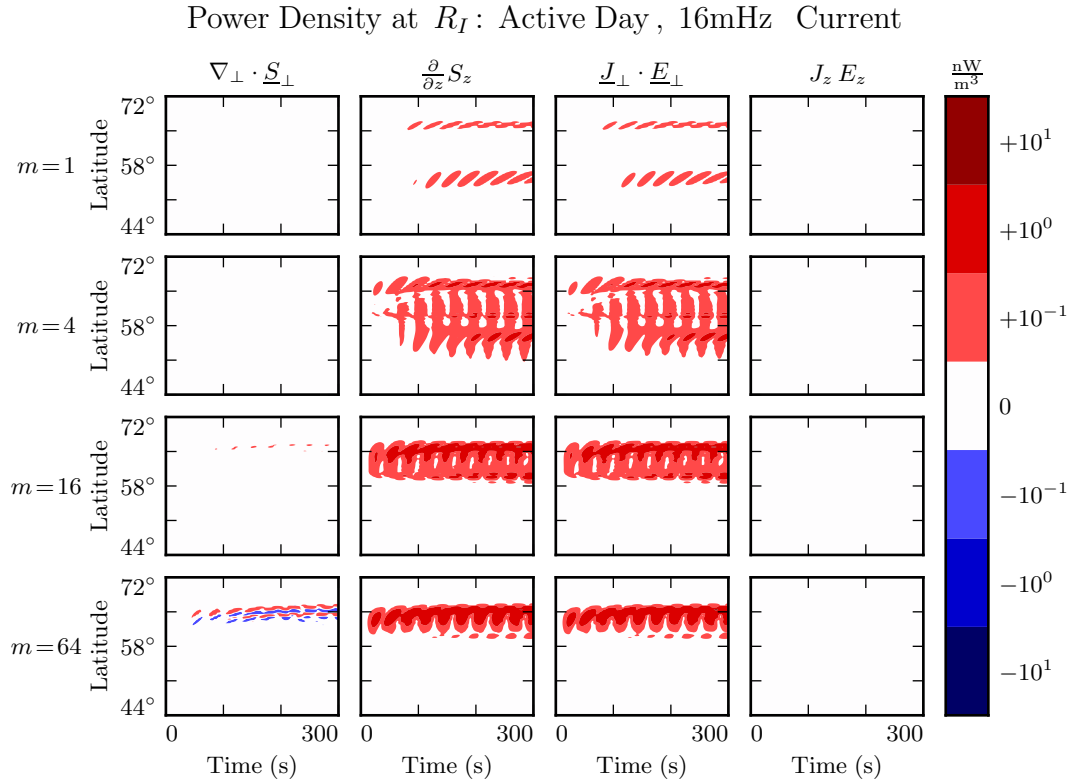


Figure 2.10: TODO: While field-aligned currents can be of significant size, they are not particularly good at depositing energy in the ionosphere. Energy deposited by the Poynting flux matches closely with Joule dissipation from the perpendicular currents – energy conservation! – while  $J_{\parallel} E_{\parallel}$  is smaller by several orders of magnitude.

according to the model, parallel currents and electric fields do not contribute significantly.

### 2.3.3 Inertial Length Scales

TODO: We do a few runs which sorta resolve the electron inertial length. It's about 2 km, and we get resolution down to 0.7 km. This is a factor of ten increase in resolution, and an additional factor of ten decrease in the time step (due to the drop in Alfvén crossing time). It's not enough. FIG is clearly not well-resolved. Those wiggles are

Parallel Electric Fields: Quiet Day, 100s of 16mHz Current,  $m = 16$

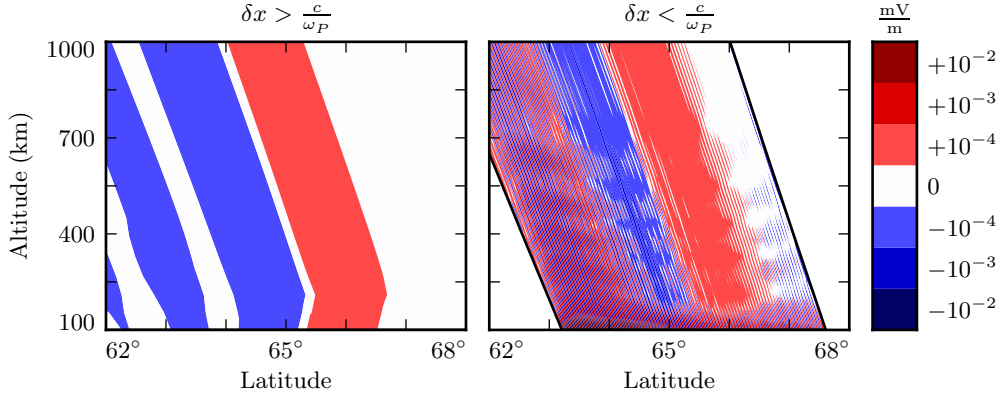


Figure 2.11: The parallel electric field develops significant structure when the perpendicular grid resolution is smaller than the electron inertial length. Unfortunately, such runs are prohibitively expensive. The lower panel – which still fails to resolve wave structure properly – represents a 100-fold increase in computational time.

probably about to cause a crash.

test reference: Figure 2.11 Figure 2.10

**TODO:** Note, again, that only the figures in the present chapter include electron inertia. Those in Chapters 3 and 4 do not, for the sake of stability and computational cost.

With a bit of algebra, the meridional components of the dispersion tensor from Section 2.1.3 provide a comparison of the parallel and perpendicular electric field magnitudes.

$$\frac{E_{\parallel}}{E_{\perp}} = \frac{-k_{\parallel}k_{\perp}c^2}{\omega^2 - k_{\perp}^2c^2 - \omega_P^2} \sim \frac{k^2c^2}{\omega_P^2} \quad (2.63)$$

### 2.3.4 Field-Aligned Current

**TODO:** The field-aligned current activity lines up with the Poynting flux. Poloidal Poynting flux is calculated from real  $E_y$  and  $B_x$ . Toroidal Poynting flux is imaginary  $E_x$  and  $B_y$ . The real component of the field-aligned current matches up with the poloidal,

and the imaginary component lines up with the toroidal.

TODO: Over the bulk of the simulation, each field is overwhelmingly either real or imaginary. However, that gets muddled at the ionosphere by the Hall conductivity (rather than being purely a function of azimuthal derivatives).

TODO: Notably, while the net Poynting flux is downward almost everywhere, field-aligned currents alternate between upward and downward flow. Perhaps this has to do with Poynting flux being a quadratic quantity while current is linear?

The “wiggles” visible in the lower-left corner of Figure 2.9 suggests overcorrection due to an improperly-coarse grid. See Section 2.3.3.

TODO: Field-aligned currents can be of significant size, but they’re not particularly good at depositing energy in the ionosphere. As would be expected from energy conservation,  $\nabla \cdot \underline{S}$  closely resembles  $\underline{J} \cdot \underline{E}$ , but only a vanishingly small portion of that is due to  $J_z E_z$ .

TODO: Are we really computing the electric fields faithfully? As touched on in Section 2.3.2, the perpendicular wavelength is important for determining the strength of the parallel electric field. This is because everything depends on derivatives, not magnitudes.

The electron inertial length  $\frac{c}{\omega_P}$  is on the order of 1 km, smaller than the wavelength of a field line resonance by three or four orders of magnitude. That is, at high altitude, the parallel electric field is expected to be smaller than the perpendicular electric field by a factor of  $10^7$  – perhaps more, depending on how closely the wave vector is aligned to the magnetic field. That seems fine – note that Figure 2.8 shows that  $\max E_{\parallel}$  is 4 to 5 orders larger than  $\max E_{\perp}$ ... plus high altitude is the parallel field’s minimum and the perpendicular field’s maximum.

TODO: A typical run has maximum perpendicular electric field on the order of 10 mV/m. Maybe a bit more. Field structures vary on the order of as little as  $\sim 1^\circ$ . That could give up to  $\nabla \times \underline{E} \sim 10^2$  nT/s. In comparison parallel electric fields max out around  $10^{-3}$  mV/m. If that varies as a scale of the inertial length – as we expect, recalling Section 2.3.1 – that’s order of 1 km, it could give  $\nabla \times \underline{E} \sim 1$  nT/s. Plausibly large

enough to have a visible effect. Note that the electron inertial length only needs to be resolved in the perpendicular direction, since that's where we're taking curls of the parallel electric field... which is the only quantity expected to change significantly (to lowest order) as a result of electron inertial effects.

TODO: This poses a significant computational cost. Within the plasmasphere, the inertial length is on the order of 0.1 km. That's two-plus orders of magnitude smaller than the present grid. Moving the inner boundary from  $L = 2$  to  $L = 5$  makes up half of that.

TODO: The moral of the present section is that proper handling of electron inertial effects will probably show additional structure at small scales... but that simulating those structures is computationally expensive in terms of computational expense, even in 2.5D.

## Chapter 3

# Results

TODO: This chapter is the real moneymaker. The overarching motivation for this work is that Pc4 pulsations vary in interesting ways with respect to azimuthal modenumber, and that prior models have been unable to give a good picture of that behavior.

### 3.1 Finite Poloidal Lifetimes

Radoski[88] looked at Alfvén waves, using a cylindrical coordinate system to imitate an “unwrapped” dipole. He argued that poloidal waves should asymptotically rotate to the toroidal mode.

Mann[71] performed some wave-in-a-box simulations and found the rotation time to be linear in modenumber:  $\tau = \frac{d\lambda}{d\omega'_A}$ , where  $\lambda = \frac{m}{2\pi r}$  and  $\omega'_A$  is the spatial derivative of the Alfvén bounce frequency. Soon afterwards[72], he supported his simulations analytically.

**TODO:** Crunch out  $\frac{d\lambda}{d\omega'_A}$ . Preliminary indications are that it doesn’t translate well to a realistic grid, but let’s double check.

Ding[20] ran simulations more or less concurrent with Mann’s. Ding saw a rotation from poloidal to toroidal... then back again. It seems that the reversal was a spatial resolution issue.

The aforementioned models made significant simplifying assumptions in terms of geometry and boundary conditions.

Mann used straight field lines, a uniform Alfvén speed gradient, and perfectly conducting boundaries.

Ding’s simulation is nominally carried out in a dipole geometry, but the ionospheric boundary is at  $2.5 R_E$ . Boundaries are also perfectly conducting.

That is, the results below offer a significantly higher level of realism than any past simulation (in part, of course, because computers are a lot better than they were 20 years ago).

A dedicated 3D treatment of this problem is unlikely at present. Large azimuthal modenumbers are expensive to compute. That’s the whole point!

The energy is obtained by integrating (using the Jacobian to handle the grid properly)  $U = \int dU = \int u dV$ . Values are the log (base 10) of that, in the slightly odd units of gigajoules per radian. A factor of  $2\pi$  wouldn’t change anything, of course, but it seems inappropriate to integrate all the way around the sphere when Pc4s are longitudinally localized (a fact which was an important part of justifying a 2.5D approach).

### 3.1.1 High Conductivity

In Figure 3.1, the rotation of energy from the poloidal mode to the toroidal mode is clear. Driving is strictly poloidal, yet the toroidal mode accumulates energy over time, and doesn't appear to give it back. The rotation happens faster for low- $m$  simulations, qualitatively consistent with Mann's result; the time at which poloidal and toroidal energies are equal seems to even be linear in  $m$ , in line with his result.

At least, this is the case on the dayside, where the ionosphere is highly conductive.

Poloidal (Blue) and Toroidal (Red) Energy: Active Day

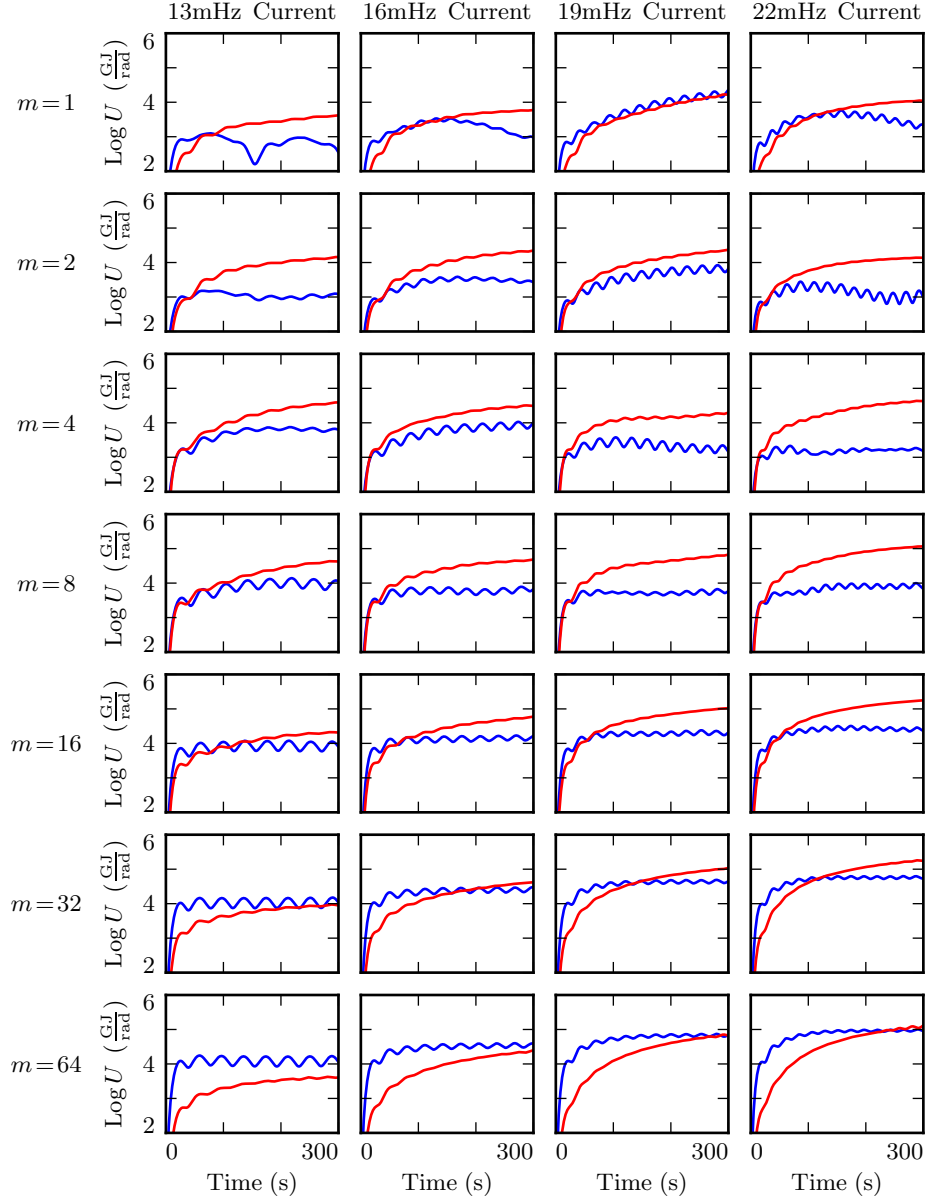


Figure 3.1: Driving – delivered to the poloidal mode – asymptotically rotates to the toroidal mode. The rate of rotation is strongly affected by the azimuthal modenumber.

TODO: Talk about why this is exciting.

TODO: Note that Mann looked specifically at second-harmonic waves.

TODO: This result shows agreement with – and significant refinement of – Mann’s findings. In the case of large-but-finite ionospheric conductivity, dipole geometry, and realistic Alfvén speed profile, energy does asymptotically rotate from the poloidal mode to the toroidal mode. The rotation rate is strongly affected by azimuthal modenumber and, in the case of large-but-finite  $m$ , has a characteristic timescale in the tens of periods. The present work furthermore demonstrates that the rotation rate is affected by driving frequency (did Mann talk about this at all, or just work in normalized time?)

### 3.1.2 Low Conductivity

The picture on the nightside (where the ionospheric conductivity is low) is significantly different from the dayside (where it’s high).

Dissipation seems to outstrip rotation. Energy does not accumulate over numerous driving periods, as would be expected in resonance; it follows the driving up and down, as a damped-driven oscillator.

There is evidence that the rotation is still trying to happen. At low  $m$ , energy is distributed between the poloidal and toroidal mode before dissipating; at high  $m$ , the energy dissipates straight out of the poloidal mode, never having had a chance to rotate.

Poloidal (Blue) and Toroidal (Red) Energy: Quiet Night

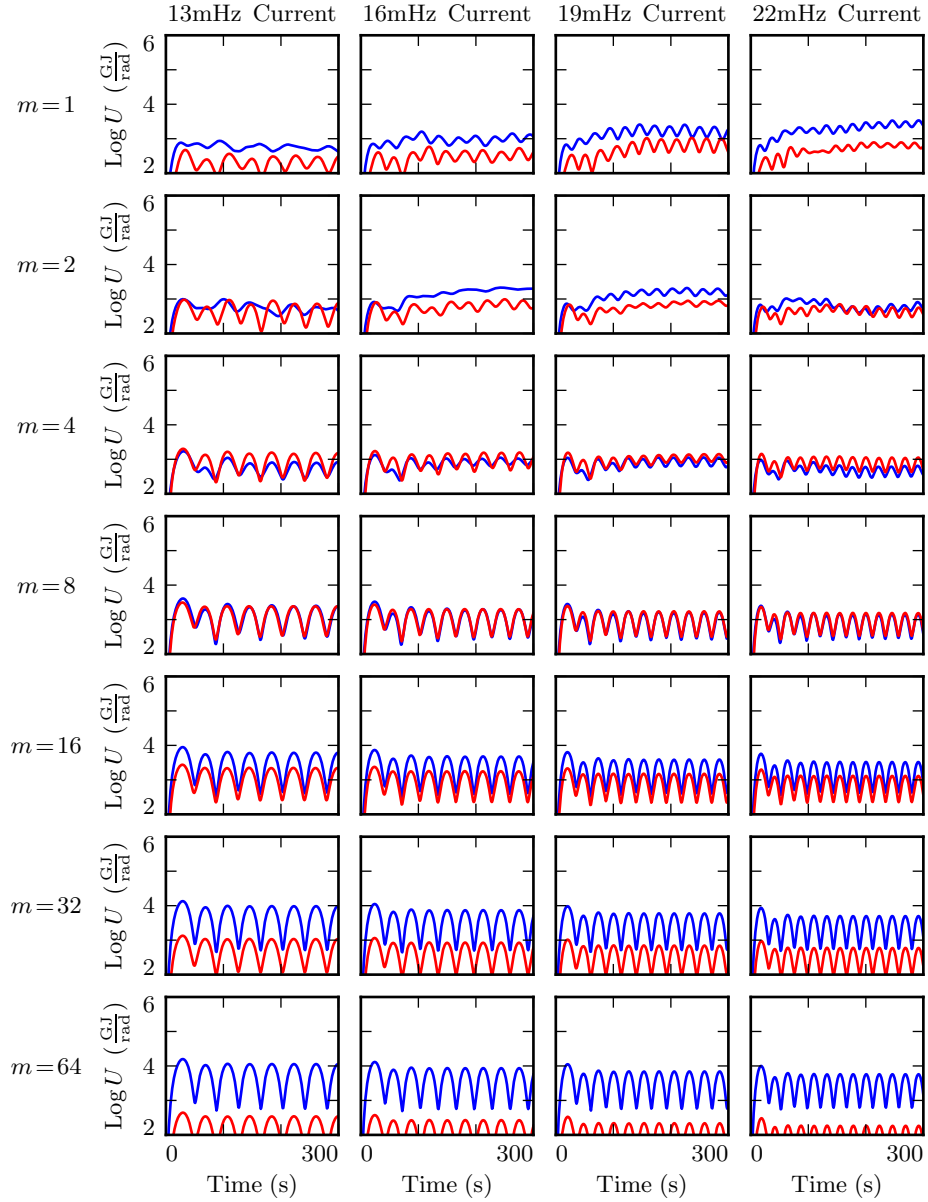


Figure 3.2: Driving is applied to the poloidal electric field. There is some rotation of energy to the toroidal mode (and less at high azimuthal modenumber), but the low ionospheric conductivity prevents energy from accumulating over time.

TODO: Why is this exciting?

TODO: Previous considerations of poloidal lifetimes have been limited to the high conductivity regime. The present work demonstrates that the low conductivity regime exhibits qualitative differences. Ionospheric conductivity on the nightside is low enough that resonance does not develop, even in the case of ongoing driving. The dissipation timescale is comparable to the rotation timescale. Rather than asymptotically accumulating energy in the toroidal mode, the oscillator asymptotically oscillates following the driving. This is relevant to the question of day-night asymmetry in the observation of field line resonances.

## 3.2 Spatial Distribution of Energy

Looking a bit deeper, it's possible to comment on the structure of the poloidal and toroidal modes, not just their magnitudes. The following commentary addresses the dayside; on the nightside, there's never much by the way of resonance.

In Figures 3.3 and 3.4, electromagnetic energy is binned by field line, averaged over volume (again, with respect to the Jacobian), and plotted as contours. All plots share a color scale.

The poloidal mode and the toroidal mode exhibit qualitatively different behavior, related to the fact that energy rotates from poloidal to toroidal, and not back.

At low  $m$ , energy rotates out of the poloidal mode so quickly that no resonance can form.

At high  $m$ , the Alfvén wave is guided. If the driving frequency lines up with the resonant frequency where it's delivered, the poloidal mode resonates strongly. Otherwise, again, no energy accumulates.

In no case does the poloidal mode demonstrate the ability to move energy across magnetic field lines.

On the other hand, the toroidal mode does resonate, even if the driving isn't resonant (though in that case the response is of course stronger). The toroidal mode transports energy across field lines until it encounters resonance, then accumulates energy there. Often, resonances are seen in multiple locations due to the non-monotonic Alfvén bounce frequency (recall Figure 1.1) as a function of  $L$ .



### 3.2.1 Resonant Driving

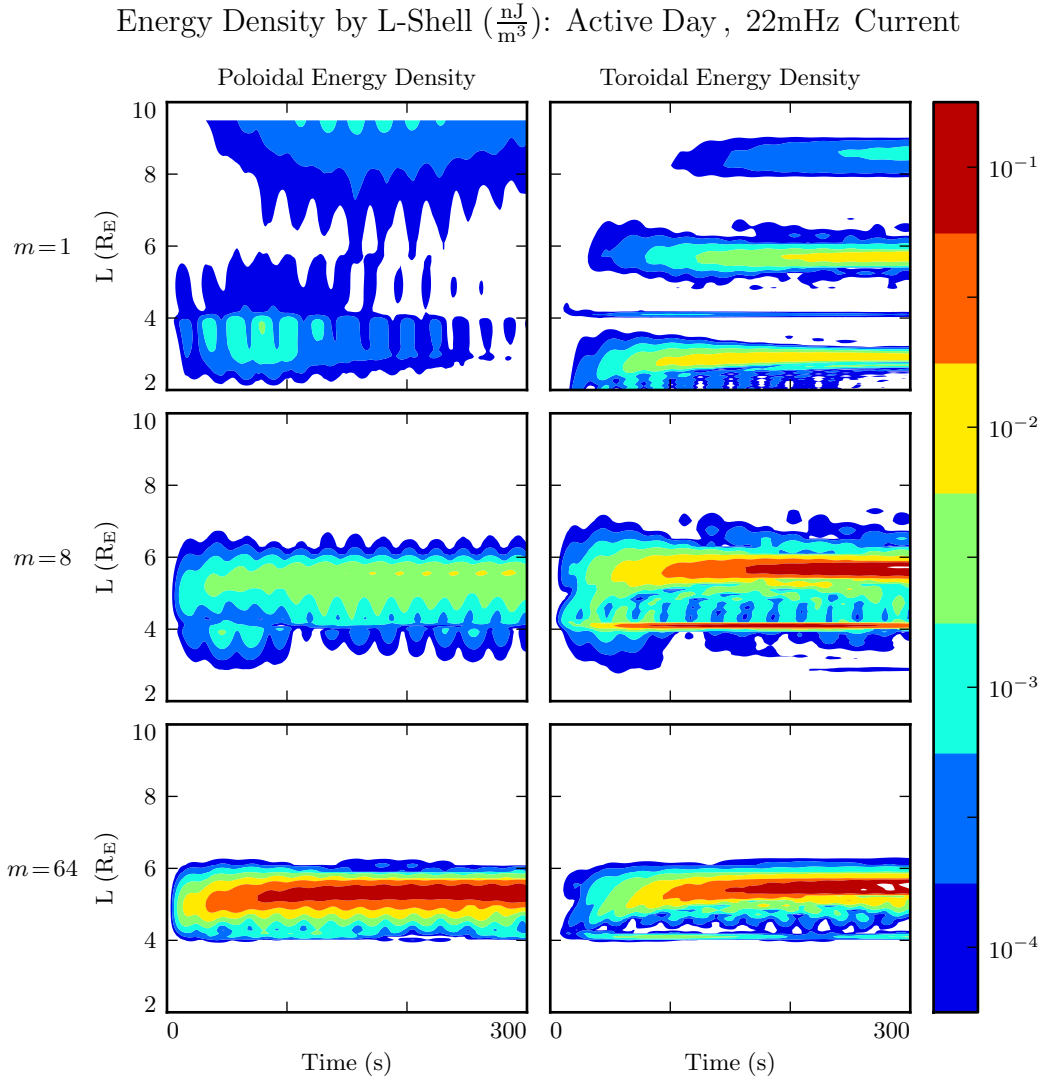


Figure 3.3: If  $m$  is small, energy rotates to the toroidal mode too fast to form a poloidal resonance. If  $m$  is large, the Alfvén wave is guided, so it resonates only if the driving frequency lines up with the resonant frequency where it's applied. The result is just one big – or perhaps even giant – pulsation. If the driving lines up with a nearby field line, the toroidal mode goes crazy! Resonance inside the plasmasphere. Resonance at the plasmapause. Resonance at the driving location. And (weak) attempt at a higher harmonic further out.

TODO: Why is this exciting?

TODO: Driving from inside the magnetosphere is novel.



### 3.2.2 Nonresonant Driving

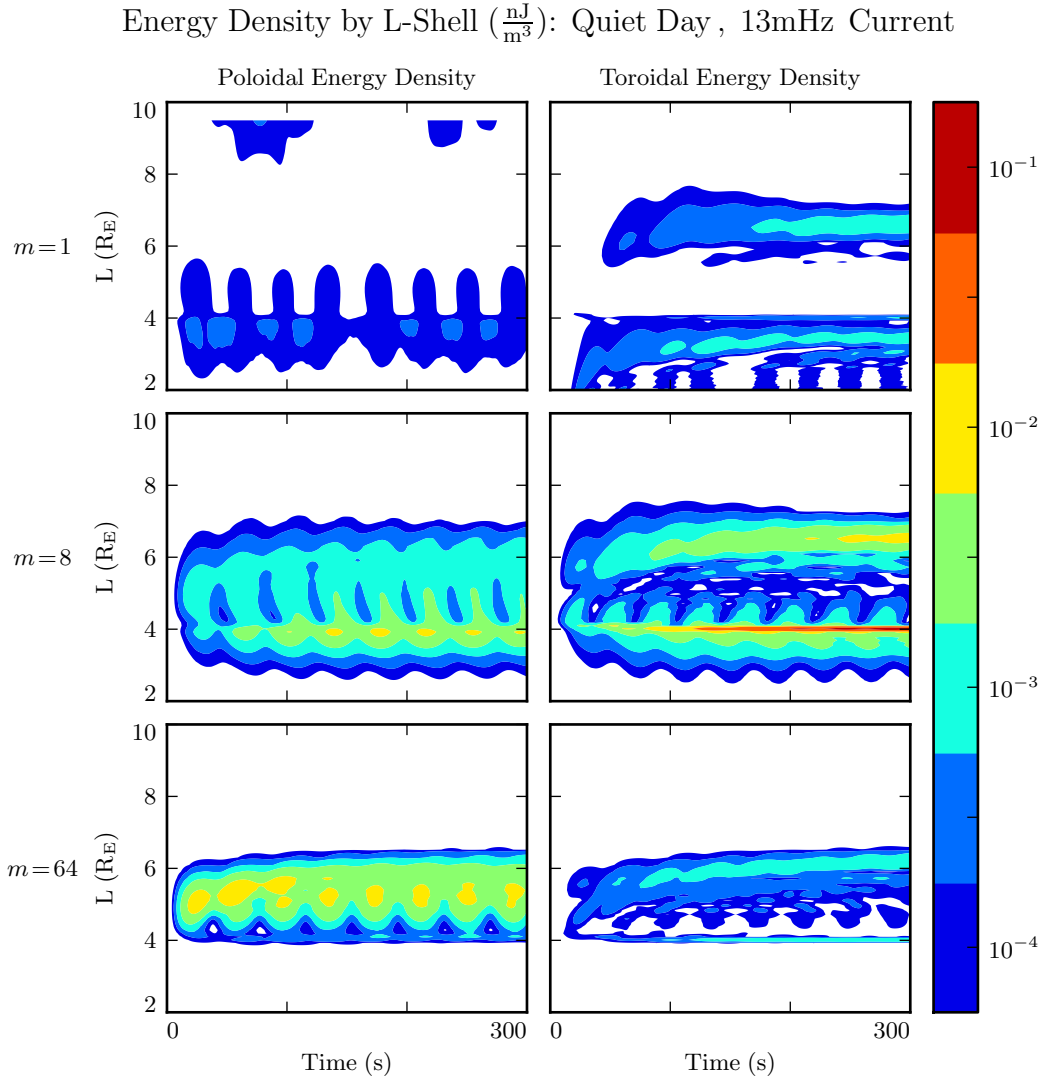


Figure 3.4: When the driving frequency doesn't line up with the location where it's delivered, there's basically no response. There is no movement of energy to a resonant field line, so no energy can accumulate over the course of multiple rounds of driving. Even when not driven resonantly, the toroidal mode still makes the best of its situation. It steals what energy it can from the poloidal mode, carries it to the resonant  $L$ -shell, and gets to work. (In contrast, recall from Figure 3.3, in this situation the poloidal mode just does not accumulate energy.) 68

TODO: Why is this exciting?

### 3.3 Significance for Giant Pulsations

Giant pulsations are (probably[101]) fundamental mode poloidal  $Pc4$  pulsations with frequencies around 10 mHz and azimuthal modenumber around 20. They are large, and can sometimes be observed on the ground.

While this model makes no particular distinction between a giant pulsation and any other  $Pc4$ , the above results do line up with giant pulsation observations.

Giant pulsations aren't seen at small  $m$ . As shown in Section 3.1, low- $m$  poloidal modes rotate to the toroidal mode too quickly to resonate effectively, even in the case of continuous driving at a locally-resonant frequency. The sweet spot seems to be around  $m = 20$ , more or less the same point where resonance becomes visible in Figure 3.3. Admittedly, giant pulsations are typically closer to 10 mHz than 22 mHz. It seems likely that qualitatively similar results would be encountered if the driving were moved to an  $L$ -shell with a bounce time of 10 mHz.

#### 3.3.1 Ground Signatures

**TODO:** [101] talks significantly about the east-west polarization.

Giant pulsations are seen at very large  $m$ , though not on the ground[102], due to damping by the ionosphere.

Giant pulsations are most common on the dayside (particularly the morningside), during geomagnetically quiet times. Giant pulsation ground signatures are noted for their predisposition towards east-west polarization.

In Figure 3.5, the strongest east-west ground signatures is obtained on the geomagnetically quiet dayside, at  $m$  of 16 and 32.

This seems to be a giant pulsation "sweet spot": the poloidal mode becomes stronger as  $m$  increases, but the ionospheric damping also increases.

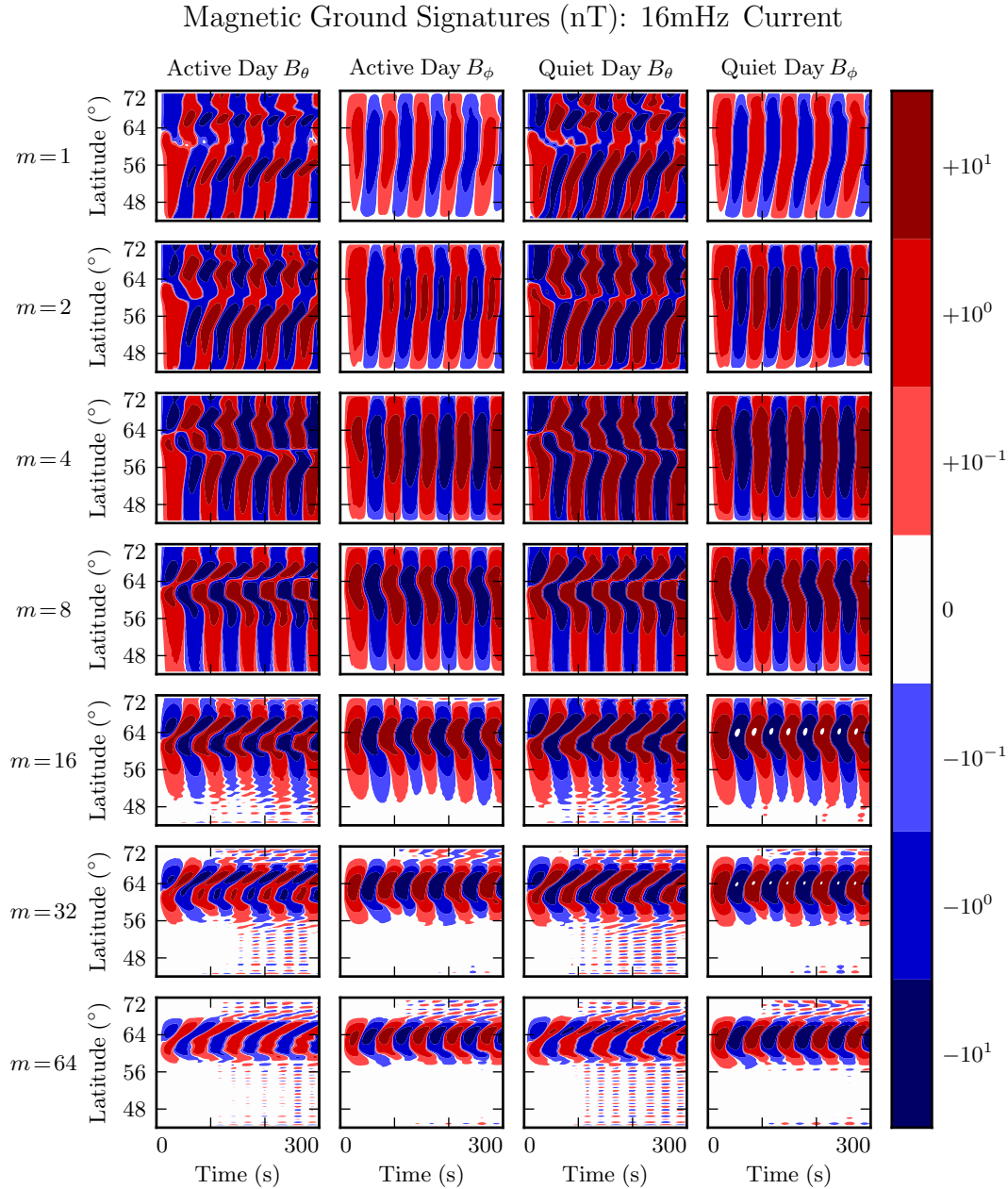


Figure 3.5: The east-west component of magnetic ground signatures is peaked on the geomagnetically quiet dayside, at modenumbers around 16 to 32. This coincides nicely with observations of giant pulsations. Like the east-west component, the north-south ground signature is strongest on the quiet dayside; however, unlike the east-west component, the north-south component is weak when the modenumber is large.

Giant pulsations are monochromatic, and can be accompanied by “multiharmonic toroidal waves”[101]. Per Section 3.2, this is about what would be expected from a mishmash of poloidal driving. Poloidal modes of all frequencies rotate into the toroidal mode; resonant poloidal modes resonate; non-resonant poloidal modes become evanescent.

Giant pulsations often drift azimuthally. This model can’t resolve azimuthal drift directly, of course, but can fake it by looking at complex phase. There has been some indication (not shown) of complex phase rotation in ground magnetic fields. However, at the boundary, it’s difficult to disentangle which values are imaginary to indicate an azimuthal offset, and which are imaginary because of Hall coupling. Investigation is ongoing.

# Chapter 4

## Observations

TODO: Talk about recent surveys by Dai[15] and Motoba[75]. Note that they skirt the issue of the fundamental mode in general. Everyone talks about how Pgs are rare... but how rare are they compared to the fundamental poloidal Pc4 in general?

## 4.1 Event Selection

Note that, in gathering his 860 events, Dai[15] did not take the  $\underline{E} \cdot \underline{B} = 0$  assumption to clean up the electric field data. The present work has taken that assumption – and discarded all events within  $15^\circ$  of the probe’s spin axis.

This cuts it down to ... events.

Furthermore distinguish the fundamental mode from the second harmonic...

Insist on a certain confidence...

### 4.1.1 Identifying the Fundamental Harmonic

Takahashi[102] spells this out explicitly. Fundamental mode, south of the equator, V should lead B by 90 degrees.

Per Takahashi[101], phase lag can be used to distinguish the fundamental harmonic from the second harmonic.

Chisham and Orr[12] argue that around  $7 R_E$ , frequency around 10 mHz precludes higher harmonics. Or maybe look at [36]?

Green[35] and Cummings[13] talk about the frequencies for ideal toroidal modes.

Dai[15] says to look at [101] and [16] for unambiguous identification of the fundamental mode.

[63] talks about setting the coordinate system using the time-averaged magnetic field, and the azimuthal direction being  $\hat{B}_0 \times \hat{r}$ .

### 4.1.2 Bias in MLT

Because RBSP’s spin plane faces the Sun, it can’t get good electric field data at dawn or dusk. Let’s plot the fraction of time at each hour of MLT that the data is unusable.

## 4.2 Something Something Results

**TODO:** Collections of events at a single ground observatory (near  $66^\circ$ ) over significant periods of time:

Brekke[7] looked at 523 giant pulsation events recorded at Tromsø, Norway, from 1929 to 1985. This spanned several solar cycles.

Rolf[89] collected 28 events between 1921 and 1930 at Abisko.

Sucksdorf[96] got 150 events between 1914 and 1938 in Sodankylä.

Harang[?]. 97 events from 1929 to 1941. Also Tromsø. Note that this may have been limited by the war!

This comes out to something like ... events over ... years. That's about ... giant pulsations per year, observed on the ground.

**TODO:** Collections of events at an array of ground observatories:

Chisham and Orr[12] found 34 events from 1984 to 1987 using the EISCAT magnetometer array in Scandinavia. About  $5^\circ$  in MLT, decent coverage from  $63^\circ$  to  $67^\circ$  mlat. This coincides with a solar minimum.

Motoba, in 2015, recorded 105 giant pulsation events. The observations were carried out by a number of ground magnetometers spanning  $\sim 90^\circ$  in local time and ranging roughly  $60^\circ$  to  $70^\circ$  magnetic latitude[75]. This was mostly during a period of low solar activity, so we expect a high count.

**TODO:** Estimate of the size of an event's footprint:

Velkamp[110] looked at a single large event and showed that, at best, it was visible over a span of  $5^\circ$  in magnetic latitude.

This is seemingly consistent with the 29 February 2012 event discussed in detail by Motoba[75] – Motoba shows some data, but doesn't discuss this aspect in detail.

Takahashi[101] computes a FWHM of about 1 in L, or  $2^\circ$  magnetic latitude.

**TODO:** Tying that in to RBSP observations?

Note that it's a bit tricky to compare ground observations to in situ observations. Large- $m$  events won't make it through the ionosphere.

There should be no bias with respect to MLT between a ground magnetometer and RBSP. Dai's analysis was specifically chosen to take advantage of the fact that RBSP's orbit had precessed all the way around the Earth. No preferred direction. And mlat shouldn't cause issues... these are FLRs, after all.

How strong does an event need to be on the ground, or in the sky, to count as a giant pulsation? Motoba 2015[75] has an event which tops out on the order of 10 nT on the ground. It's more like 5 mV/m in situ. Takahashi[101] has similar values.

Note that Takahashi[102] has shown that it's OK to call something a giant pulsation even if it's not visible on the ground... though, obviously, we are comparing to ground magnetometer data for occurrence rate.

If peak Pg observations are at  $66^\circ$  mlat, that corresponds to  $L = 6$ . Then let's suppose that peak Pg viewing is  $5^\circ$  wide – estimating from the work of Velkamp and Motoba. That means RBSP should see lots of Pgs when it's between  $L = 5.2$  and  $L = 7.1$ . Well,  $7.1 R_E$  is outside its apogee, but the probes spend a fair amount of time outside  $L = 5.2$ , since they are moving pretty slowly at that point.

Giant pulsations have been shown to be more numerous in times of low solar activity. That was the whole point of Brekke's seminal 1987 paper, and it's consistent with what we show in Section 3.3. The RBSP observations occur during peak solar times, though it's an anemic solar peak[83].

**TODO:** How much time does RBSP spend outside of  $L = 5.2$  (for a range of  $5^\circ$ )? How about  $L = 5.6$  to  $L = 6.5$  (for FWHM of  $2^\circ$ )?

Each RBSP probe spends about 30 % of its orbit between  $L = 5.6$  and  $L = 6.5$ .

RBSP-A and RBSP-B count as two observers. In one  $\sim 5$  cases out of hundreds do they simultaneously observe a poloidal Pc4 event (although, most notably for the 2012 event which [16] considers in detail), both probes do fly through the same apparent event several hours apart from one another.

The duration of Dai's survey is October 2012 to June 2014. Scaled by 2 probes, each

of which is present in the peak Pg lshells 30% of the time, that comes out to almost exactly one year.

TODO: How many fundamental mode poloidal events do we see? How many could pass for giant pulsations? How many should we expect to see?

TODO: How weird is it for a fundamental mode poloidal Pc4 to be monochromatic?

TODO: How weird is it for a fundamental mode poloidal Pc4 to be stronger than 5 mV/m at the equator?

#### 4.2.1 Something Something Results

## **Chapter 5**

## **Conclusion**

## 5.1 Summary of Results

TODO: Write this.

## 5.2 Future Work

Arbitrary deformation of grid. Get  $\hat{e}_i = \frac{\partial}{\partial u^i} \underline{x}$ , then  $g_{ij} = \hat{e}_i \cdot \hat{e}_j$ , then invert the metric tensor for contravariant components.

MPI. Some benchmarks with time to compute vs time to broadcast. At what problem scale does additional parallelization make sense?

Driving based on events? Wouldn't be that hard.

Test particles? Seems silly. Watching something drift-bounce resonate will require making assumptions about what's going on on the other face of the planet.

Conductivity affected by precipitation/current?

IRI ionosphere model. Solar illumination effects.

# References

- [1] S.-I. Akasofu. The development of the auroral substorm. *Planetary and Space Science*, 12(4):273–282, 1964.
- [2] B. J. Anderson. An overview of spacecraft observations of 10s to 600s period magnetic pulsations in Earth’s magnetosphere. In M. J. Engebretson, K. Takanashi, and M. Scholer, editors, *Solar Wind Sources of Magnetospheric Ultra-Low-Frequency Waves*, volume 81 of *Geophys. Monogr.*, pages 25–43. American Geophysical Union, Washington, DC, 1994.
- [3] B. J. Anderson, M. J. Engebretson, S. P. Rounds, L. J. Zanetti, and T. A. Potemra. A statistical study of Pc 3-5 pulsations observed by the AMPTE/CCE magnetic fields experiment, 1. occurrence distributions. *J. Geophys. Res.*, 95(A7):10495, 1990.
- [4] C. W. Arthur and R. L. McPherron. The statistical character of Pc 4 magnetic pulsations at synchronous orbit. *J. Geophys. Res.*, 86(A3):1325, 1981.
- [5] K. Birkeland. Expédition norvégienne de 1899-1900 pour l’étude des aurores boréales. *Mat. Naturvidensk. Kl.*, KI(I), 1901.
- [6] J. P. Boris. A physically motivated solution of the Alfvén problem. *NRL Memorandum Report*, 2167, 1970.
- [7] A. Brekke, T. Feder, and S. Berger. Pc4 giant pulsations recorded in Tromsø, 1929-1985. *Journal of Atmospheric and Terrestrial Physics*, 49(10):1027–1032, 1987.

- [8] A. A. Chan, M. Xia, and L. Chen. Anisotropic alfvén-balloon modes in Earth's magnetosphere. *J. Geophys. Res. Space Physics*, 99(A9):17351–17366, 1994.
- [9] L. Chen and A. Hasegawa. A theory of long-period magnetic pulsations: 1. steady state excitation of field line resonance. *J. Geophys. Res.*, 79(7):1024–1032, 1974.
- [10] L. Chen and A. Hasegawa. Kinetic theory of geomagnetic pulsations: 1. internal excitations by energetic particles. *J. Geophys. Res.*, 96(A2):1503, 1991.
- [11] C. Z. Cheng and Q. Qian. Theory of ballooning-mirror instabilities for anisotropic pressure plasmas in the magnetosphere. *J. Geophys. Res.*, 99(A6):11193, 1994.
- [12] G. Chisham and D. Orr. Statistical studies of giant pulsations (pgs): Harmonic mode. *Planetary and Space Science*, 39(7):999–1006, 1991.
- [13] W. D. Cummings, R. J. O'Sullivan, and P. J. Coleman. Standing Alfvén waves in the magnetosphere. *J. Geophys. Res.*, 74(3):778–793, 1969.
- [14] L. Dai. Collisionless magnetic reconnection via Alfvén eigenmodes. *Phys. Rev. Lett.*, 102(24), 2009.
- [15] L. Dai, K. Takahashi, R. Lysak, C. Wang, J. R. Wygant, C. Kletzing, J. Bonnell, C. A. Cattell, C. W. Smith, R. J. MacDowall, S. Thaller, A. Breneman, X. Tang, X. Tao, and L. Chen. Storm time occurrence and spatial distribution of Pc4 poloidal ULF waves in the inner magnetosphere: A Van Allen Probes statistical study. *J. Geophys. Res. Space Physics*, 120:4748–4762, 2015.
- [16] L. Dai, K. Takahashi, J. R. Wygant, L. Chen, J. Bonnell, C. A. Cattell, S. Thaller, C. Kletzing, C. W. Smith, R. J. MacDowall, D. N. Baker, J. B. Blake, J. Fennell, S. Claudepierre, H. O. Funsten, G. D. Reeves, and H. E. Spence. Excitation of poloidal standing Alfvén waves through drift resonance wave-particle interaction. *Geophys. Res. Lett.*, 40:4127–4132, 2013.
- [17] A. W. Degeling, R. Rankin, and Q.-G. Zong. Modeling radiation belt electron acceleration by ULF fast mode waves, launched by solar wind dynamic pressure fluctuations. *J. Geophys. Res. Space Physics*, 119(11):8916–8928, 2014.

- [18] R. E. Denton, M. F. Thomsen, K. Takahashi, R. R. Anderson, and H. J. Singer. Solar cycle dependence of bulk ion composition at geosynchronous orbit. *J. Geophys. Res.*, 116(A3), 2011.
- [19] W. D. D'haeseleer, W. N. G. H. J. D. Callen, and J. L. Shohet. *Flux Coordinates and Magnetic Field Structure*. Springer-Verlag, New York, 1991.
- [20] D. Q. Ding, R. E. Denton, M. K. Hudson, and R. L. Lysak. An MHD simulation study of the poloidal mode field line resonance in the Earth's dipole magnetosphere. *J. Geophys. Res.*, 100:63–77, 1995.
- [21] J. W. Dungey. The attenuation of Alfvén waves. *J. Geophys. Res.*, 59(3):323–328, 1954.
- [22] A. Einstein. Die grundlage der allgemeinen relativitätstheorie. *Ann. Phys.*, 354:769–822, 1916.
- [23] S. R. Elkington. Resonant acceleration and diffusion of outer zone electrons in an asymmetric geomagnetic field. *J. Geophys. Res.*, 108(A3), 2003.
- [24] S. R. Elkington, M. K. Hudson, and A. A. Chan. Acceleration of relativistic electrons via drift-resonant interaction with toroidal-mode Pc-5 ULF oscillations. *Geophys. Res. Lett.*, 26(21):3273–3276, 1999.
- [25] M. J. Engebretson, D. L. Murr, K. N. Erickson, R. J. Strangeway, D. M. Klumpar, S. A. Fuselier, L. J. Zanetti, and T. A. Potemra. The spatial extent of radial magnetic pulsation events observed in the dayside near synchronous orbit. *J. Geophys. Res.*, 97(A9):13741, 1992.
- [26] M. J. Engebretson, L. J. Zanetti, T. A. Potemra, W. Baumjohann, H. Lühr, and M. H. Acuna. Simultaneous observation of Pc 34 pulsations in the solar wind and in the Earth's magnetosphere. *J. Geophys. Res. Space Physics*, 92:10053–10062, 1987.
- [27] M. J. Engebretson, L. J. Zanetti, T. A. Potemra, D. M. Klumpar, R. J. Strangeway, and M. H. Acuña. Observations of intense ULF pulsation activity near the geomagnetic equator during quiet times. *J. Geophys. Res.*, 93(A11):12795, 1988.

- [28] P. T. I. Eriksson, L. G. Blomberg, A. D. M. Walker, and K.-H. Glassmeier. Poloidal ULF oscillations in the dayside magnetosphere: a Cluster study. *Ann. Geophys.*, 23(7):2679–2686, 2005.
- [29] S. Fujita and T. Tamao. Duct propagation of hydromagnetic waves in the upper ionosphere, 1, electromagnetic field disturbances in high latitudes associated with localized incidence of a shear Alfvén wave. *J. Geophys. Res.*, 93(A12):14665, 1988.
- [30] K.-H. Glassmeier. Magnetometer array observations of a giant pulsation event. *J. Geophys.*, 48:127–138, 1980.
- [31] K.-H. Glassmeier. On the influence of ionospheres with non-uniform conductivity distribution on hydromagnetic waves. *J. Geophys.*, 54(2):125–137, 1984.
- [32] K.-H. Glassmeier, S. Buchert, U. Motschmann, A. Korth, and A. Pedersen. Concerning the generation of geomagnetic giant pulsations by drift-bounce resonance ring current instabilities. *Ann. Geophysicae*, 17:338–350, 1999.
- [33] K.-H. Glassmeier, D. Klimushkin, C. Othmer, and P. Mager. ULF waves at mercury: Earth, the giants, and their little brother compared. *Advances in Space Research*, 33(11):1875–1883, 2004.
- [34] K.-H. Glassmeier and M. Stellmacher. Concerning the local time asymmetry of Pc5 wave power at the ground and field line resonance widths. *J. Geophys. Res.*, 105(A8):18847–18855, 2000.
- [35] C. A. Green. Observations of Pg pulsations in the northern auroral zone and at lower latitude conjugate regions. *Planetary and Space Science*, 27(1):63–77, 1979.
- [36] C. A. Green. Giant pulsations in the plasmasphere. *Planetary and Space Science*, 33(10):1155–1168, 1985.
- [37] J. L. Green and S. Boardsen. Duration and extent of the great auroral storm of 1859. *Advances in Space Research*, 38(2):130–135, 2006.
- [38] C. Greifinger and P. S. Greifinger. Theory of hydromagnetic propagation in the ionospheric waveguide. *J. Geophys. Res.*, 73(23):7473–7490, 1968.

- [39] G. Haerendel, W. Baumjohann, E. Georgescu, R. Nakamura, L. M. Kistler, B. Klecker, H. Kucharek, A. Vaivads, T. Mukai, and S. Kokubun. High-beta plasma blobs in the morningside plasma sheet. *Ann. Geophys.*, 17(12):1592–1601, 1999.
- [40] B. C. Hall. *Lie Groups, Lie Algebras, and Representations*. Graduate Texts in Mathematics. Springer, New York, second edition, 2015.
- [41] Y. X. Hao, Q.-G. Zong, Y. F. Wang, X.-Z. Zhou, H. Zhang, S. Y. Fu, Z. Y. Pu, H. E. Spence, J. B. Blake, J. Bonnell, J. R. Wygant, and C. A. Kletzing. Interactions of energetic electrons with ULF waves triggered by interplanetary shock: Van allen probes observations in the magnetotail. *J. Geophys. Res. Space Physics*, 119(10):8262–8273, 2014.
- [42] A. Hasegawa. Drift-wave instability at the plasmapause. *J. Geophys. Res.*, 76(22):5361–5364, 1971.
- [43] O. Hillebrand, J. Muench, and R. L. McPherron. Ground-satellite correlative study of a giant pulsation event. *Journal of Geophysics Zeitschrift Geophysik*, 51:129–140, 1982.
- [44] W. J. Hughes. The effect of the atmosphere and ionosphere on long period magnetospheric micropulsations. *Planet. Space Sci.*, 22:1157–1172, 1974.
- [45] W. J. Hughes. Magnetospheric ULF waves: A tutorial with a historical perspective. In M. J. Engebretson, K. Takahashi, and M. Scholer, editors, *Solar Wind Sources of Magnetospheric Ultra-Low-Frequency Waves*, volume 81 of *Geophys. Monogr.*, pages 1–12. American Geophysical Union, Washington, DC, 1994.
- [46] W. J. Hughes and D. J. Southwood. The screening of micropulsation signals by the atmosphere and ionosphere. *J. Geophys. Res.*, 81(19):3234–3240, 1976.
- [47] W. J. Hughes, D. J. Southwood, B. Mauk, R. L. McPherron, and J. N. Barfield. Alfvén waves generated by an inverted plasma energy distribution. *Nature*, 275(5675):43–45, 1978.
- [48] J. A. Jacobs, Y. Kato, S. Matsushita, and V. A. Troitskaya. Classification of geomagnetic micropulsations. *J. Geophys. Res.*, 69(1):180–181, 1964.

- [49] A. N. Jaynes, M. R. Lessard, K. Takahashi, A. F. Ali, D. M. Malaspina, R. G. Michell, E. L. Spanswick, D. N. Baker, J. B. Blake, C. Cully, E. F. Donovan, C. A. Kletzing, G. D. Reeves, M. Samara, H. E. Spence, and J. R. Wygant. Correlated Pc45 ULF waves, whistler-mode chorus, and pulsating aurora observed by the Van Allen Probes and ground-based systems. *J. Geophys. Res. Space Physics*, 120:87498761, 2015.
- [50] Y. Kato and T. Tsutomu. Hydromagnetic oscillations in a conducting medium with hall conduct-ivity under the uniform magnetic field. *Science reports of the Tohoku University. Ser. 5, Geophysics*, 7(3):147–164, 1956.
- [51] M. C. Kelley. *The Earth’s Ionosphere*. Academic Press, San Diego, second edition, 1989.
- [52] R. L. Kessel. Solar wind excitation of pc5 fluctuations in the magnetosphere and on the ground. *J. Geophys. Res.*, 113(A4), 2008.
- [53] M. G. Kivelson. Ulf waves from the ionosphere to the outer planets. In K. Takahashi, P. J. Chi, R. E. Denton, and R. L. Lysak, editors, *Magnetospheric ULF Waves: Synthesis and New Directions*, volume 169 of *Geophys. Monogr.*, pages 11–30. American Geophysical Union, Washington, DC, 2006.
- [54] D. Y. Klimushkin. Resonators for hydromagnetic waves in the magnetosphere. *J. Geophys. Res.*, 103(A2):2369–2375, 1998.
- [55] D. Y. Klimushkin, P. N. Mager, and K.-H. Glassmeier. Toroidal and poloidal Alfvén waves with arbitrary azimuthal wavenumbers in a finite pressure plasma in the earth’s magnetosphere. *Annales Geophysicae*, 22(1):267–287, 2004.
- [56] S. Kokubun. Observations of Pc pulsations in the magnetosphere: Satellite-ground correlation. *J. Geomagn. Geoelec*, 32(Supplement2):SII17–SII39, 1980.
- [57] S. Kokubun, K. N. Erickson, T. A. Fritz, and R. L. McPherron. Local time asymmetry of Pc 4-5 pulsations and associated particle modulations at synchronous orbit. *J. Geophys. Res.*, 94(A6):6607–6625, 1989.
- [58] D.-H. Lee. On the generation mechanism of pi 2 pulsations in the magnetosphere. *Geophys. Res. Lett.*, 25(5):583–586, 1998.

- [59] D.-H. Lee and K. Kim. Compressional MHD waves in the magnetosphere: A new approach. *J. Geophys. Res.*, 104(A6):12379–12385, 1999.
- [60] A. S. Leonovich and V. A. Mazur. Structure of magnetosonic eigenoscillations of an axisymmetric magnetosphere. *J. Geophys. Res.*, 105(A12):27707–27715, 2000.
- [61] W. Liu, J. B. Cao, X. Li, T. E. Sarris, Q.-G. Zong, M. Hartinger, K. Takahashi, H. Zhang, Q. Q. Shi, and V. Angelopoulos. Poloidal ULF wave observed in the plasmasphere boundary layer. *J. Geophys. Res. Space Physics*, 118(7):4298–4307, 2013.
- [62] W. Liu, T. E. Sarris, X. Li, S. R. Elkington, R. Ergun, V. Angelopoulos, J. Bonnell, and K. H. Glassmeier. Electric and magnetic field observations of Pc4 and Pc5 pulsations in the inner magnetosphere: A statistical study. *J. Geophys. Res.*, 114(A12), 2009.
- [63] W. Liu, T. E. Sarris, X. Li, R. Ergun, V. Angelopoulos, J. Bonnell, and K. H. Glassmeier. Solar wind influence on Pc4 and Pc5 ULF wave activity in the inner magnetosphere. *J. Geophys. Res.*, 115(A12), 2010.
- [64] W. Liu, T. E. Sarris, X. Li, Q.-G. Zong, R. Ergun, V. Angelopoulos, and K. H. Glassmeier. Spatial structure and temporal evolution of a dayside poloidal ULF wave event. *Geophys. Res. Lett.*, 38(19), 2011.
- [65] R. L. Lysak. Magnetosphere-ionosphere coupling by Alfvén waves at midlatitudes. *J. Geophys. Res.*, 109, 2004.
- [66] R. L. Lysak and D. hun Lee. Response of the dipole magnetosphere to pressure pulses. *Geophys. Res. Lett.*, 19(9):937–940, 1992.
- [67] R. L. Lysak and Y. Song. A three-dimensional model of the propagation of Alfvén waves through the auroral ionosphere: first results. *Adv. Space Res.*, 28:813–822, 2001.
- [68] R. L. Lysak, C. L. Waters, and M. D. Sciffer. Modeling of the ionospheric Alfvén resonator in dipolar geometry. *J. Geophys. Res. Space Physics*, 118, 2013.

- [69] P. N. Mager and D. Y. Klimushkin. Giant pulsations as modes of a transverse Alfvénic resonator on the plasmapause. *Earth, Planets and Space*, 65(5):397–409, 2013.
- [70] I. R. Mann, E. A. Lee, S. G. Claudepierre, J. F. Fennell, A. Degeling, I. J. Rae, D. N. Baker, G. D. Reeves, H. E. Spence, L. G. Ozeke, R. Rankin, D. K. Milling, A. Kale, R. H. W. Friedel, and F. Honary. Discovery of the action of a geophysical synchrotron in the Earth’s Van Allen radiation belts. *Nature Communications*, 4, 2013.
- [71] I. R. Mann and A. N. Wright. Finite lifetimes of ideal poloidal Alfvén waves. *J. Geophys. Res.*, 100:23677–23686, 1995.
- [72] I. R. Mann, A. N. Wright, and A. W. Hood. Multiple-timescales analysis of ideal poloidal Alfvén waves. *J. Geophys. Res.*, 102(A2):2381–2390, 1997.
- [73] T. Maynard, N. Smith, S. Gonzalez, et al. Solar storm risk to the North American electric grid. 2013.
- [74] R. L. McPherron, G. K. Parks, D. S. Colburn, and M. D. Montgomery. Satellite studies of magnetospheric substorms on august 15, 1968: 2. solar wind and outer magnetosphere. *J. Geophys. Res.*, 78(16):3054–3061, 1973.
- [75] T. Motoba, K. Takahashi, J. V. Rodriguez, and C. T. Russell. Giant pulsations on the afternoonside: Geostationary satellite and ground observations. *J. Geophys. Res. Space Physics*, 120:8350–8367, 2015.
- [76] NASA. Coordinated data analysis (workshop) web.
- [77] NASA. Near miss: The solar superstorm of july 2012.
- [78] M. Nicolet. The collision frequency of electrons in the ionosphere. *Journal of Atmospheric and Terrestrial Physics*, 3(4):200–211, 1953.
- [79] A. Nishida. Ionospheric screening effect and storm sudden commencement. *Journal of Geophysical Research*, 69(9):1861–1874, 1964.

- [80] L. G. Ozeke and I. R. Mann. Modeling the properties of high-m Alfvén waves driven by the drift-bounce resonance mechanism. *J. Geophys. Res.*, 106(A8):15583–15597, 2001.
- [81] L. G. Ozeke and I. R. Mann. Energization of radiation belt electrons by ring current ion driven ULF waves. *J. Geophys. Res.*, 113(A2), 2008.
- [82] L. G. Ozeke, I. R. Mann, K. R. Murphy, I. J. Rae, D. K. Milling, S. R. Elkington, A. A. Chan, and H. J. Singer. ULF wave derived radiation belt radial diffusion coefficients. *J. Geophys. Res.*, 117(A4), 2012.
- [83] W. D. Pesnell. Predictions of solar cycle 24: How are we doing? *Space Weather*, 14(1):10–21, 2016.
- [84] E. M. Poulter, W. Allan, E. Nielsen, and K.-H. Glassmeier. Stare radar observations of a PG pulsation. *J. Geophys. Res.*, 88(A7):5668, 1983.
- [85] J. A. Proehl, W. Lotko, I. Kouznetsov, and S. D. Geimer. Ultralow-frequency magnetohydrodynamics in boundary-constrained geomagnetic flux coordinates. *J. Geophys. Res.*, 107(A9):1225, 2002.
- [86] H. R. Radoski. Highly asymmetric MHD resonances: the guided poloidal mode. *J. Geophys. Res.*, 72(15), 1967.
- [87] H. R. Radoski. A note on oscillating field lines. *J. Geophys. Res.*, 72(1), 1967.
- [88] H. R. Radoski. A theory of latitude dependent geomagnetic micropulsations: The asymptotic fields. *J. Geophys. Res.*, 79, 1974.
- [89] B. Rolf. Giant micropulsations at abisko. *J. Geophys. Res.*, 36(1):9, 1931.
- [90] G. Rostoker, H.-L. Lam, and J. V. Olson. PC 4 giant pulsations in the morning sector. *J. Geophys. Res.*, 84(A9):5153, 1979.
- [91] C. T. Russell, J. G. Luhmann, T. J. Odera, and W. F. Stuart. The rate of occurrence of dayside Pc 3,4 pulsations: The L-value dependence of the IMF cone angle effect. *Geophys. Res. Lett.*, 10(8):663–666, 1983.

- [92] D. G. Sibeck, G. Korotova, D. L. Turner, V. Angelopoulos, K.-H. Glassmeier, and J. P. McFadden. Frequency doubling and field-aligned ion streaming in a long-period poloidal pulsation. *J. Geophys. Res.*, 117(A11), 2012.
- [93] H. J. Singer, W. J. Hughes, and C. T. Russell. Standing hydromagnetic waves observed by ISEE 1 and 2: Radial extent and harmonic. *J. Geophys. Res.*, 87(A5):3519, 1982.
- [94] D. J. Southwood. Some features of field line resonances in the magnetosphere. *Planetary and Space Science*, 22(3):483–491, 1974.
- [95] D. J. Southwood. A general approach to low-frequency instability in the ring current plasma. *J. Geophys. Res.*, 81(19):3340–3348, 1976.
- [96] E. Sucksdorff. Giant pulsations recorded at sodankyl during 19141938. *Terrestrial Magnetism and Atmospheric Electricity*, 44(2):157–170, 1939.
- [97] K. Takahashi, D. Berube, D.-H. Lee, J. Goldstein, H. J. Singer, F. Honary, and M. B. Moldwin. Possible evidence of virtual resonance in the dayside magnetosphere. *J. Geophys. Res.*, 114(A5), 2009.
- [98] K. Takahashi, J. Bonnell, K.-H. Glassmeier, V. Angelopoulos, H. J. Singer, P. J. Chi, R. E. Denton, Y. Nishimura, D.-H. Lee, M. Nosé, and W. Liu. Multipoint observation of fast mode waves trapped in the dayside plasmasphere. *J. Geophys. Res.*, 115(A12), 2010.
- [99] K. Takahashi, R. E. Denton, W. Kurth, C. Kletzing, J. Wygant, J. Bonnell, L. Dai, K. Min, C. W. Smith, and R. MacDowall. Externally driven plasmaspheric ULF waves observed by the Van Allen Probes. *J. Geophys. Res. Space Physics*, 120(1):526–552, 2015.
- [100] K. Takahashi, J. F. Fennell, E. Amata, and P. R. Higbie. Field-aligned structure of the storm time Pc 5 wave of november 14–15, 1979. *J. Geophys. Res.*, 92(A6):5857, 1987.
- [101] K. Takahashi, K.-H. Glassmeier, V. Angelopoulos, J. Bonnell, Y. Nishimura, H. J. Singer, and C. T. Russell. Multisatellite observations of a giant pulsation event. *J. Geophys. Res.*, 116:A11223, 2011.

- [102] K. Takahashi, M. D. Hartinger, V. Angelopoulos, K.-H. Glassmeier, and H. J. Singer. Multispacecraft observations of fundamental poloidal waves without ground magnetic signatures. *J. Geophys. Res. Space Physics*, 118:4319–4334, 2013.
- [103] K. Takahashi, R. W. McEntire, A. T. Y. Lui, and T. A. Potemra. Ion flux oscillations associated with a radially polarized transverse Pc 5 magnetic pulsation. *J. Geophys. Res.*, 95(A4):3717, 1990.
- [104] K. Takahashi and R. L. McPherron. Standing hydromagnetic oscillations in the magnetosphere. *Planetary and Space Science*, 32:1343–1359, 1984.
- [105] K. Takahashi, N. Sato, J. Warnecke, H. Lühr, H. E. Spence, and Y. Tonegawa. On the standing wave mode of giant pulsations. *J. Geophys. Res. Space Physics*, 97(A7):10717–10732, 1992.
- [106] T. Tamao. Transmission and coupling resonance of hydromagnetic disturbances in the non-uniform Earth’s magnetosphere. *Sci. Rept. Tohoku Univ.*, 17(2):43, 1965.
- [107] S. M. Thompson and M. G. Kivelson. New evidence for the origin of giant pulsations. *J. Geophys. Res.*, 106(A10):21237–21253, 2001.
- [108] W. Tu, S. R. Elkington, X. Li, W. Liu, and J. Bonnell. Quantifying radial diffusion coefficients of radiation belt electrons based on global MHD simulation and spacecraft measurements. *J. Geophys. Res.*, 117(A10), 2012.
- [109] A. Vaivads, W. Baumjohann, G. Haerendel, R. Nakamura, H. Kucharek, B. Klecker, M. R. Lessard, L. M. Kistler, T. Mukai, and A. Nishida. Compressional Pc5 type pulsations in the morningside plasma sheet. *Ann. Geophys.*, 19(3):311–320, 2001.
- [110] J. Veldkamp. A giant geomagnetic pulsation. *Journal of Atmospheric and Terrestrial Physics*, 17(4):320–324, 1960.
- [111] C. L. Waters, R. L. Lysak, and M. D. Sciffer. On the coupling of fast and shear Alfvén wave modes by the ionospheric Hall conductance. *Earth Planets Space*, 65:385–396, 2013.

- [112] C. L. Waters and M. D. Sciffer. Field line resonant frequencies and ionospheric conductance: Results from a 2-d MHD model. *J. Geophys. Res.*, 113(A5), 2008.
- [113] D. M. Wright and T. K. Yeoman. High-latitude HF doppler observations of ULF waves: 2. waves with small spatial scale sizes. *Ann. Geophys.*, 17(7):868–876, 1999.
- [114] B. Yang, Q.-G. Zong, Y. F. Wang, S. Y. Fu, P. Song, H. S. Fu, A. Korth, T. Tian, and H. Reme. Cluster observations of simultaneous resonant interactions of ULF waves with energetic electrons and thermal ion species in the inner magnetosphere. *J. Geophys. Res.*, 115(A2), 2010.
- [115] K. Yee. Numerical solution of initial boundary value problems involving maxwell's equations in isotropic media. *IEEE Trans. Antennas Propagat.*, 14(3), 1966.
- [116] T. K. Yeoman and D. M. Wright. ULF waves with drift resonance and drift-bounce resonance energy sources as observed in artificially-induced HF radar backscatter. *Ann. Geophys.*, 19(2):159–170, 2001.
- [117] Q.-G. Zong, X.-Z. Zhou, X. Li, P. Song, S. Y. Fu, D. N. Baker, Z. Y. Pu, T. A. Fritz, P. Daly, A. Balogh, and H. Réme. Ultralow frequency modulation of energetic particles in the dayside magnetosphere. *Geophys. Res. Lett.*, 34(12), 2007.
- [118] Q.-G. Zong, X.-Z. Zhou, Y. F. Wang, X. Li, P. Song, D. N. Baker, T. A. Fritz, P. W. Daly, M. Dunlop, and A. Pedersen. Energetic electron response to ULF waves induced by interplanetary shocks in the outer radiation belt. *J. Geophys. Res.*, 114(A10), 2009.

## Appendix A

# Differential Geometry

TODO: Not sure that a glossary or list of acronyms will be necessary, but here are the examples from the template.

### A.1 Glossary

- **Cosmic-Ray Muon (CR  $\mu$ )** – A muon coming from the abundant energetic particles originating outside of the Earth's atmosphere.

### A.2 Acronyms

Table A.1: Acronyms

Acronym	Meaning
CR $\mu$	Cosmic-Ray Muon